

Robust Cislunar Low-Thrust Trajectory Optimization under Uncertainties via Sequential Covariance Steering

Naoya Kumagai* and Kenshiro Oguri†
Purdue University, West Lafayette, Indiana, 47907

Spacecraft operations are influenced by uncertainties such as dynamics modeling, navigation, and maneuver execution errors. Although mission design has traditionally incorporated heuristic safety margins to mitigate the effect of uncertainties, particularly before/after crucial events, it is yet unclear whether this practice will scale in the cislunar region, which features locally chaotic nonlinear dynamics and involves frequent lunar flybys. This paper applies chance-constrained covariance steering and sequential convex programming to simultaneously design an optimal trajectory and trajectory correction policy that can probabilistically guarantee safety constraints under the assumed physical/navigational error models. The results show that the proposed method can effectively control the state uncertainty in a highly nonlinear environment and provide a trajectory with better local stability properties than a trajectory designed without considering uncertainties. The framework allows faster computation and lossless covariance propagation compared to existing methods, enabling a rapid and accurate comparison of ΔV_{99} costs for different uncertainty parameters. We demonstrate the algorithm on several transfers in the Earth-Moon Circular Restricted Three Body Problem.

I. Introduction

Mission operations are subject to various uncertainties, such as unmodeled accelerations, orbit determination, maneuver execution errors, missed thrust events, and launch errors. Especially in cislunar space, a challenging environment that features greater dynamics nonlinearities that skew any Gaussian state uncertainties into non-Gaussian, there is an increasing interest in effectively characterizing the uncertainties through orbit determination [1] and uncertainty quantification [2]. Also of interest is the design of control strategies that address these uncertainties.

Compared to traditional mission design which involves heuristic margins for increased safety, especially after crucial events such as planetary gravity assists and launch, operations in cislunar space will encounter far more frequent crucial events, the representative one being lunar flybys. With a higher frequency of such events, heuristic safety margins may

An earlier version of this paper was presented as paper 24-379 at the 2024 AAS/AIAA Astrodynamics Specialist Conference, Broomfield, CO, August 11-15 2024.

*Ph.D. Student, School of Aeronautics and Astronautics, Purdue University, West Lafayette, Indiana, 47907; nkumagai@purdue.edu (Corresponding author)

†Assistant Professor, School of Aeronautics and Astronautics, Purdue University, West Lafayette, Indiana, 47907.

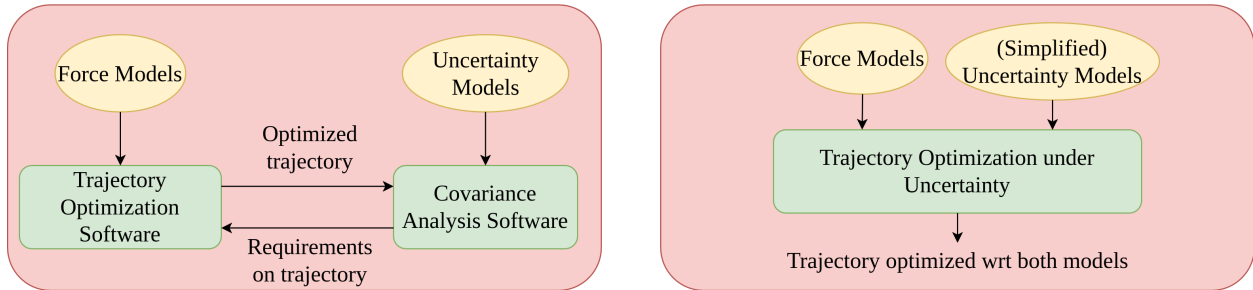


Fig. 1 Comparison of a typical mission design process (left) vs trajectory optimization process that also takes into account the uncertainty models (right).

be overly time-consuming to incorporate or even make the transfer designs infeasible. These scenarios call for a higher level of automation in the safe trajectory design process that introduces less conservativeness in the safety margins. The trajectory and control (i.e. trajectory correction maneuver (TCM)) policy should ideally be designed with the underlying uncertainty models in mind to reduce conservativeness. Figure 1 shows a comparison of a typical mission design process and trajectory optimization that takes into account the uncertainty models. The traditional mission design process involves an iteration process between the trajectory design and uncertainty analysis, where uncertainty analysis may inform the trajectory design on where to add safety margins. The trajectory is then designed with the safety margins, and the uncertainty analysis is performed again to check if the safety margins are sufficient; generally, this process is repeated several times, which can be time-consuming. On the other hand, the proposed method involves a trajectory optimization process that also takes into account the uncertainty models. While the uncertainty models that are used in the optimization process may not be of the same fidelity as dedicated uncertainty analysis tools, the optimization process can provide a more direct way to design a trajectory that is robust to uncertainties without the need for an iterative process.

A promising and rapidly expanding approach for designing safe controllers that can also provide non-conservative solutions is stochastic optimal control (SOC), which directly considers the state probability distribution in the optimization process. Several recent works have addressed SOC in the context of deep-space trajectory design, with varying uncertainty quantification (UQ) and optimization methods. Differential dynamic programming (DDP) and unscented transform (UT) are combined in [3, 4] to design closed-loop feedback policies for low-thrust trajectory design. While an explicit control policy is unavailable from these works and fitting from sigma points is required to retrieve the policy, [5] provides an explicit linear feedback policy. Greco et al. [6] includes orbit determination errors and uses nonlinear programming (NLP) for constructing robust open-loop impulsive trajectories. The algorithm utilizes a Gaussian Mixture Model (GMM) to approximate the state distribution, offering a high-fidelity UQ capability not seen in other methods. At the same time, the method relies on finite differencing inside the NLP solver; the complexity of the problem makes it seemingly difficult to obtain analytical gradients to further improve the method. Methods that use

linear covariance analysis (LinCov) as a lower-level covariance propagation technique, in combination with various optimization techniques at the top level, have also been proposed in the literature. For example, [7] uses a genetic algorithm, [8] uses particle swarm optimization, and [9] uses a Sweeping Gradient Method [10]. Several methods based on primer vector theory also exist; for example, [11] considers the covariance as an additional state variable, and [12] proposes a control law that explicitly modifies the costate.

Methods based on sequential convex programming (SCP), dynamics linearization, and linear covariance propagation are proposed in [13–16]. Ridderhof et al. [13] was one of the first works of the SCP approaches; Oguri and Lantoine [15] additionally consider orbit determination and mass uncertainty, as well as multi-phase mission design. Benedikter et al. [14] proposes a different convexification scheme. Although its proof of lossless convexification was shown to be incorrect [17], similar methods have been recently proposed for linear systems [18, 19]. These linearization-based approaches can be broadly classified into two categories: methods that explicitly define the state covariance as decision variables [14], which we term the *full covariance* formulations, and methods that implicitly optimize for the covariance by constructing a large block matrix that is analogous to the Cholesky decomposition of covariance matrices [13, 15], which we term the *block Cholesky* formulations. An inherent drawback in the *block Cholesky* formulation is the required computational effort; although each subproblem is a convex program, it involves solving a large Linear Matrix Inequality, the size of which scales quadratically with the number of discretization nodes. On the other hand, the *full covariance* formulation subproblem is computationally more efficient due to the empirical linear growth of the computational complexity with respect to the number of nodes, which has been demonstrated for linear systems [19]. Recent works on rendezvous and proximity operations have considered rotational motion [20, 21], navigation-enhancing maneuvers [22]. Works that consider non-Gaussian uncertainties via Gaussian mixture models for linear systems are also emerging [23, 24].

To summarize the rapidly growing number of SOC approaches, we provide a comparison in Table 1, based on the aspects that influence the fidelity, optimality, and computational effort. ‘UQ’ compares the uncertainty quantification fidelity; ‘Control Policy Optimization’ compares whether the method can output an optimized control policy. Navigation uncertainty is also a dividing factor that is an unignorable aspect of space trajectory optimization and is included. ‘Gradient Information’ refers to the method in which the algorithm accesses derivative information; DDP-based methods inherently utilize up to the second-order derivative of the dynamics (state transition matrix (STM) and tensor (STT)), along with sigma points through unscented transform. SCP-based methods, by linearizing the dynamics and formulating the subproblem as a convex optimization, take advantage of highly optimized interior-point solvers that essentially perform the task of gradient evaluation. Finally, we provide a comparison of the main computational efforts that limit the algorithm complexity; the computational time for the SCP and indirect-based methods are based on the authors’ previous work.

SOC has been demonstrated in cislunar space, mainly for stationkeeping on periodic orbits in the Circular Restricted

Table 1 Comparison of Stochastic Optimal Control Approaches for Space Trajectory Optimization

Ref.	Method	UQ (Fidelity)	Control Policy Optimization	Considers Navigation Uncertainty	Gradient Information	Main Computational Effort (Time)
[4]	DDP	UT (Med.)	yes (fitting at σ points)	no	STM, STT, and σ points	requires nonlin. σ point propagation (unclear)
[5]	DDP	UT (Med.)	yes (linear feedback on state deviation)	yes	STM, STT, and σ points	requires nonlin. σ point propagation (hours [5])
[13, 15]	SCP (block Chol.)	LinCov (Low)	yes (linear feedback on state deviation)	no [13] yes [15]	linearization & discretization; leverages convex solver	solves large LMI (hours)
[14]	SCP (full cov)	LinCov (Low)	yes (linear feedback on state history deviation /stochastic process) See Remark 5.	no	linearization & discretization; leverages convex solver	solves multiple small LMIs (seconds to minutes)
[6]	NLP (finite diff.)	GMM (High)	no (B-plane targeter in-the-loop)	yes	Ref. uses finite diff.; availability of analytical derivative unclear	unclear
[11]	Indirect	LinCov (Low)	no (open-loop)	no	Ref. uses finite diff.	solves 2PBVP for mean and covariance (minutes)

Three Body Problem (CR3BP)[16]. However, there is a gap in the literature on applications to general transfers. This paper adds to the literature of SCP-based SOC methods, with applications to designing a nominal robust trajectory and TCM policy for transfers in cislunar space. The main contributions are threefold. First, we show one of the first demonstrations of the SCP-based SOC method in cislunar space which is applicable for both low-thrust and impulsive propulsion systems. The method is capable of modeling unmodeled dynamics, maneuver execution errors, orbit determination errors, and initial insertion errors, and computing an state estimate-linear TCM policy that can explicitly account for the state covariance. The SOC approach is shown to effectively control the state uncertainty in an environment featuring high nonlinearity. Numerical examples of DRO-to-DRO and NRHO-to-Halo transfers demonstrate the effectiveness of the method. Second, we formulate a variant of the *full covariance* formulation that formulates each subproblem as a convex problem which can be solved more efficiently than *block Cholesky* formulations and is exact in the covariance propagation (cf. [14]). We show a method of imposing 2-norm upper bound constraints on the control input, which shows smaller conservativeness than recently proposed methods. Third, analyzing the nominal trajectory obtained from the optimization under uncertainties via the local Lyapunov exponent shows that the

resulting trajectory has better local stability compared to trajectory optimization that does not consider uncertainties.

The paper is outlined as follows: Section II outlines the force model (CR3BP), uncertainty models, and the ΔV_{99} minimization problem formulation. Section III derives the filter model and the belief-space dynamics. Section IV shows the solution to the ΔV_{99} minimization problem under the assumed models via convexification and SCP. Section V shows the results of applying the algorithms to several transfers in the cislunar region and an analysis via the local Lyapunov exponent.

Notation: $\mathbb{R}, \mathbb{R}^n, \mathbb{R}^{n \times m}, \mathbb{S}^n$ represent the space of real numbers, n -dimensional real vectors, n -by- m real matrices, and symmetric n -by- n matrices, respectively. $\mathbb{P}[\cdot], \mathbb{E}[\cdot], \text{Cov}[\cdot], \|\cdot\|, \|\cdot\|_\infty, \lambda_{\max}(\cdot), \text{tr}(\cdot)$ calculate the probability, expectation, covariance, 2-norm, infinity-norm, largest eigenvalue, and trace, respectively. $A^{1/2}$ refers to any matrix such that $A^{1/2}(A^{1/2})^\top = A$. A random vector ξ with normal distribution of mean μ and covariance matrix Σ is denoted as $\xi \sim \mathcal{N}(\mu, \Sigma)$. The notation $\square_{1:k}$ denotes all elements from the first to the k -th element of the sequence. $\text{blkdiag}(\cdot, \cdot, \dots)$ denotes a block diagonal matrix with the arguments as diagonal blocks. $Q(\xi; p)$ denotes the p -quantile of the random variable ξ .

II. Problem Formulation

A. Force Model: Circular Restricted Three Body Model

For preliminary trajectory design in cislunar space, the Circular Restricted Three Body Problem (CR3BP) is a commonly-used model that can incorporate the gravitational effects of both the Earth and Moon on the spacecraft. We use this model for analysis in this work.

The CR3BP describes the motion of a particle under the gravitational influence of two bodies P_1 and P_2 , termed the primaries, with mass m_1 and m_2 , respectively. The primaries are assumed to be moving in a circular orbit around their barycenter. The particle models the spacecraft, which has an approximately infinitesimal mass compared to the primaries. We take an inertially fixed right-handed Cartesian coordinate frame with the origin at the barycenter of the two primaries. The X -axis points towards P_2 , the Z -axis is aligned with the orbital angular momentum vector of the primaries, and the Y -axis completes the right-hand system. As is done traditionally, we study the CR3BP dynamics in a length and time-nondimensionalized form. The second-order differential equations of motion (EOM) for the particle are [25]:

$$\ddot{x} - 2\dot{y} - x = -\frac{(1-\mu)(x+\mu)}{d_1^3} - \frac{\mu(x-1+\mu)}{d_2^3} \quad (1a)$$

$$\ddot{y} + 2\dot{x} - y = -\frac{(1-\mu)y}{d_1^3} - \frac{\mu y}{d_2^3} \quad (1b)$$

$$\ddot{z} = -\frac{(1-\mu)z}{d_1^3} - \frac{\mu z}{d_2^3} \quad (1c)$$

where

$$d_1 = \sqrt{(x + \mu)^2 + y^2 + z^2}, \quad d_2 = \sqrt{(x - 1 + \mu)^2 + y^2 + z^2}, \quad \mu = \frac{m_2}{m_1 + m_2} \quad (2)$$

By defining the state \mathbf{x} of the spacecraft as its position and velocity, i.e. $\mathbf{x} \in \mathbb{R}^{n_x}$, $\mathbf{x} = [x, y, z, \dot{x}, \dot{y}, \dot{z}]^\top$ with $n_x = 6$, we can express the EOM in first-order differential form. When low-thrust propulsion applies acceleration, the EOM can be written as the sum of the natural dynamics $\mathbf{f}_0(\mathbf{x})$ and the acceleration provided by the thrusters:

$$\dot{\mathbf{x}} = \mathbf{f}(\mathbf{x}, \mathbf{u}) = \mathbf{f}_0(\mathbf{x}) + \mathbf{B}\mathbf{u} \quad (3)$$

where $\mathbf{B} \in \mathbb{R}^{n_x \times n_u}$, and $\mathbf{u} \in \mathbb{R}^{n_u}$, with $n_u = 3$ and

$$\mathbf{f}_0(\mathbf{x}) = \begin{bmatrix} \dot{x} \\ \dot{y} \\ \dot{z} \\ 2\dot{y} + x - \frac{(1-\mu)(x+\mu)}{d_1^3} - \frac{\mu(x-1+\mu)}{d_2^3} \\ -2\dot{x} + y - \frac{(1-\mu)y}{d_1^3} - \frac{\mu y}{d_2^3} \\ -\frac{(1-\mu)z}{d_1^3} - \frac{\mu z}{d_2^3} \end{bmatrix}, \quad \mathbf{B} = \begin{bmatrix} \mathbf{0}_{3 \times 3} \\ \mathbf{I}_3 \end{bmatrix} \quad (4)$$

B. Uncertainty Models

1. Initial State Uncertainty

We assume knowledge about the distribution of the initial state, in terms of an initial state estimate $\hat{\mathbf{x}}_{0^-}$ and estimation error $\tilde{\mathbf{x}}_{0^-}$, both Gaussian-distributed vectors:

$$\hat{\mathbf{x}}_{0^-} \sim \mathcal{N}(\boldsymbol{\mu}_0, \hat{\mathbf{P}}_{0^-}), \quad \tilde{\mathbf{x}}_{0^-} \sim \mathcal{N}(\mathbf{0}_{n_x}, \tilde{\mathbf{P}}_{0^-}) \quad (5)$$

where $\boldsymbol{\mu}_0$ and $\hat{\mathbf{P}}_{0^-}, \tilde{\mathbf{P}}_{0^-} \geq 0$ are known.

2. Unmodeled Accelerations

We model unknown/unmodeled accelerations as a Brownian motion, which perturbs the spacecraft as an additional term in the dynamics. The spacecraft dynamics are now expressed as a stochastic differential equation (SDE):

$$d\mathbf{x} = \mathbf{f}(\mathbf{x}, \mathbf{u}) dt + \mathbf{g}(\mathbf{x}, \mathbf{u}) d\mathbf{w} \quad (6)$$

where $d\mathbf{w}(t) \in \mathbb{R}^{n_w}$ is standard Brownian motion, i.e., $\mathbb{E}[d\mathbf{w}] = \mathbf{0}_{n_w}$ and $\mathbb{E}[d\mathbf{w}(t)d\mathbf{w}^\top(t)] = I_{n_w}dt$.

3. Maneuver Execution Error

Regardless of the propulsion system, planned control maneuvers are subject to erroneous execution. In this work, we use the Gates model [26] which involves four parameters $\{\sigma_1, \sigma_2, \sigma_3, \sigma_4\}$. These respectively represent the fixed magnitude [km/s² (km/s)], proportional magnitude [%], fixed pointing [km/s² (km/s)], and proportional pointing [deg] errors for a spacecraft equipped with a low-thrust (impulsive) propulsion system. For a planned control input \mathbf{u}_k , it models the additional control error $\tilde{\mathbf{u}}_k$ as a Gaussian noise [16]:

$$\tilde{\mathbf{u}}(t) = \tilde{\mathbf{u}}_k, \quad t \in [t_k, t_{k+1}) \quad (7a)$$

$$\tilde{\mathbf{u}}_k = G_{\text{exe}}(\mathbf{u}_k)\mathbf{w}_{\text{exe},k}, \quad \mathbf{w}_{\text{exe},k} \sim \mathcal{N}(0, I_3) \quad (7b)$$

$$G_{\text{exe}}(\mathbf{u}_k) = T(\mathbf{u}_k)P_{\text{gates}}^{1/2}(\mathbf{u}_k) \quad (7c)$$

where the rotation matrix $T(\mathbf{u}_k)$ and the covariance matrix $P_{\text{gates}}(\mathbf{u}_k)$ are defined as

$$T(\mathbf{u}) = \begin{bmatrix} \hat{\mathbf{s}} & \hat{\mathbf{e}} & \hat{\mathbf{z}} \end{bmatrix}, \quad \hat{\mathbf{z}} = \frac{\mathbf{u}}{\|\mathbf{u}\|}, \quad \hat{\mathbf{e}} = \frac{[0, 0, 1]^\top \times \hat{\mathbf{z}}}{\|[0, 0, 1]^\top \times \hat{\mathbf{z}}\|}, \quad \hat{\mathbf{s}} = \hat{\mathbf{e}} \times \hat{\mathbf{z}} \quad (8)$$

$$P_{\text{gates}}(\mathbf{u}) = \begin{bmatrix} \sigma_p^2 & 0 & 0 \\ 0 & \sigma_p^2 & 0 \\ 0 & 0 & \sigma_m^2 \end{bmatrix}, \quad \sigma_m^2 = \sigma_1^2 + \sigma_2^2\|\mathbf{u}\|^2, \quad \sigma_p^2 = \sigma_3^2 + \sigma_4^2\|\mathbf{u}\|^2 \quad (9)$$

4. Orbit Determination Process

We assume that the state information is partially available through a nonlinear discrete-time observation process at the observation times t_0, t_1, \dots, t_N . The observation model is expressed as:

$$\mathbf{y}_k = \mathbf{f}_{\text{obs}}(\mathbf{x}_k) + \mathbf{g}_{\text{obs}}(\mathbf{x}_k)\mathbf{v}_k \quad (10)$$

where $\mathbf{y}_k \in \mathbb{R}^{n_y}$ is the observation, and $\mathbf{v}_k \in \mathbb{R}^{n_y}$ is an i.i.d. standard Gaussian vector. Based on the observation process, we can estimate the state and its distribution using a navigation filter. The filtering process \mathcal{F}_k is assumed to use all previous measurements $\mathbf{y}_{0:k}$ and the initial state estimate $\hat{\mathbf{x}}_{0^-}$. Then, the distribution of the state estimate $\hat{\mathbf{x}}_k$ is written as

$$\hat{\mathbf{x}}_k \sim \mathcal{F}(\hat{\mathbf{x}}_{0^-}, \mathbf{y}_{0:k}) \quad (11)$$

C. Control Policy

The control policy is a function of the state estimate, since we can only observe the state through the navigation filter:

$$\mathbf{u}(t) = \pi(\hat{\mathbf{x}}, t), \quad t \in [t_0, t_f] \quad (12)$$

D. Chance/Distributional Constraints for Safe Trajectory Design

1. Chance Constraints

When we assume a stochastic system with unbounded uncertainties such as Gaussian distributions, it is difficult to guarantee constraints on the state or control in a deterministic manner. Thus, a chance constraint generalizes the constraint $f_{\text{safe}}(\mathbf{x}, \mathbf{u}) \leq 0$ to be probabilistic in the form

$$\mathbb{P} [f_{\text{safe}}(\mathbf{x}, \mathbf{u}) \leq 0] \geq 1 - \epsilon_{cc} \quad (13)$$

where ϵ_{cc} represents the probability of chance-constraint violation, chosen as $0 < \epsilon_{cc} \ll 1$.

This work deals with chance constraints in the form of 2-norm control constraints:

$$\mathbb{P} [\|\mathbf{u}_k\| \leq u_{\max}] \geq 1 - \epsilon_u, \quad k = 0, \dots, N-1 \quad (14a)$$

where u_{\max} is a scalar upper bound on the control input 2-norm. We can also formulate more general forms of chance constraints; readers are referred to [16]. For example, keep-out zones can be imposed on the state to ensure a low probability of collision with any object.

2. Maximum Covariance Constraint

To limit the growth of the state uncertainty, we can impose a maximum covariance constraint on the state covariance at any time step k , in the form of a linear matrix inequality (LMI) constraint:

$$\text{Cov}[\mathbf{x}_k] \leq P_{\max}, \quad k = 0, \dots, N \quad (15)$$

where $P_{\max} > 0$ is a user-specified positive-definite matrix. This has another benefit of maintaining the validity of the linearization of the covariance propagation model, which is discussed in the next section.

3. Final Distributional Constraint

Similar to the chance constraints, the final state must be constrained in a probabilistic manner. Although we can impose chance constraints on the final state, we choose to impose a distributional constraint for the final state. We

constrain the mean to match a desired state $\boldsymbol{\mu}_f$ and covariance of the final state $\mathbf{x}(t_f)$ to be within a user-specified covariance matrix $P_f > 0$, i.e.

$$\mathbb{E}[\mathbf{x}(t_f)] = \boldsymbol{\mu}_f, \quad \text{Cov}[\mathbf{x}(t_f)] \leq P_f \quad (16)$$

E. Objective Function

Since our control policy is a function of the state estimate, which is a random variable, the cost function J is also a random variable. We consider the p -quantile of the cost function J as the objective function:

$$\underset{\pi}{\text{minimize}} \quad Q(J; p) \quad (17)$$

In this work, we consider the 99% quantile of the total fuel consumption as the objective function. This value is commonly termed the ΔV_{99} in spacecraft mission design:

$$J = \int_{t_0}^{t_f} \|\mathbf{u}(t)\| dt, \quad p = 0.99 \quad (18)$$

F. Original Problem Formulation

We can now formulate a chance-constrained stochastic optimal control problem as follows:

Problem 1 *Chance-Constrained ΔV_{99} Optimization (CCDVO) under Uncertainties*

$$\underset{\pi}{\text{minimize}} \quad Q\left(\int_{t_0}^{t_f} \|\mathbf{u}(t)\| dt; 0.99\right) \quad (19a)$$

$$\text{s.t.} \quad d\mathbf{x} = \mathbf{f}(\mathbf{x}, \mathbf{u}) dt + \mathbf{g}(\mathbf{x}, \mathbf{u}) d\mathbf{w} \quad \leftarrow \text{Nonlinear stochastic dynamics} \quad (19b)$$

$$\hat{\mathbf{x}}_{0^-} \sim \mathcal{N}(\boldsymbol{\mu}_0, \hat{P}_{0^-}), \quad \tilde{\mathbf{x}}_{0^-} \sim \mathcal{N}(\mathbf{0}_{n_x}, \tilde{P}_{0^-}) \quad \leftarrow \text{initial state distribution} \quad (19c)$$

$$\mathbb{P}[f_{\text{safe}}(\mathbf{x}, \mathbf{u}) \leq 0] \geq 1 - \epsilon_{cc} \quad \leftarrow \text{chance constraint} \quad (19d)$$

$$\text{Cov}[\mathbf{x}(t)] \leq P_{\max} \quad \forall t \in [t_0, t_f] \quad \leftarrow \text{maximum covariance} \quad (19e)$$

$$\mathbb{E}[\mathbf{x}(t_f)] = \boldsymbol{\mu}_f, \quad \text{Cov}[\mathbf{x}(t_f)] \leq P_f \quad \leftarrow \text{terminal distribution} \quad (19f)$$

$$\mathbf{y}_k = \mathbf{f}_{\text{obs}}(\mathbf{x}_k) + \mathbf{g}_{\text{obs}}(\mathbf{x}_k)\mathbf{v}_k \quad \leftarrow \text{observation model} \quad (19g)$$

$$\hat{\mathbf{x}}_k = \mathcal{F}(\hat{\mathbf{x}}_{0^-}, \mathbf{y}_{0:k}) \quad \leftarrow \text{navigation filter} \quad (19h)$$

$$\mathbf{u}(t) = \pi(\hat{\mathbf{x}}, t) \quad \leftarrow \text{control policy} \quad (19i)$$

Exactly solving this nonlinear stochastic optimal control problem can be computationally intractable; for example, the propagation of the state distribution through the nonlinear dynamics requires solving the Fokker-Planck equation, which can be computationally expensive. Hence, we make assumptions on the uncertainty propagation model, controller

design, and navigation filter, which are valid when the uncertainty is maintained to be small throughout the time horizon.

III. Belief-Space Dynamics and Filtered Density Propagation

In this section, we outline the assumptions on the control policy, dynamics linearization, and filtered covariance propagation model. By assuming these models, we can tractably design a closed-loop controller that explicitly takes into account the state distribution evolution.

A. Control Policy

First, we restrict the class of control policies to piecewise constant affine controllers, i.e., the control policy π is constituted by a piecewise constant control input, $\mathbf{u}_{0:N-1}$, where $\mathbf{u}(t) \equiv \mathbf{u}_k$ for $t \in [t_k, t_{k+1})$, and the control input is a linear function of the state estimate $\hat{\mathbf{x}}_k$:

$$\mathbf{u}_k = \bar{\mathbf{u}}_k + K_k(\hat{\mathbf{x}}_k - \bar{\mathbf{x}}_k) \quad (20)$$

where $\bar{\mathbf{u}}_k$ is the nominal (feedforward) control, and $K_k \in \mathbb{R}^{n_u \times n_x}$ is the feedback gain matrix, with the term $K_k(\hat{\mathbf{x}}_k - \bar{\mathbf{x}}_k)$ representing the correction to the nominal control based on the state estimate, more commonly known as TCMs in spacecraft mission design. *

Remark 1 *The linear feedback policy Eq. (20) can be regarded as a sub-optimal policy in the class of nonlinear trajectory correction policies. For example, state-of-the-art ground operations for deep-space missions typically recompute the control by solving a nonlinear trajectory optimization problem at each time step. However, since the linear feedback policy is suboptimal, it can provide a computationally tractable upper bound on the quantile cost, and can be used to estimate statistical costs for more complicated policies.*

B. Dynamics Linearization and Discretization

The uncertainty model we consider in this work takes an Extended Kalman Filter (EKF)-like model, where the first two statistical moments are considered to represent the state distribution. The state estimate mean is propagated nonlinearly through the nonlinear dynamics, while its covariance is propagated according to a linearized model. This assumption allows us to tractably design closed-loop controllers by solving an optimization that explicitly takes into account the state distribution evolution. First, we review the process of dynamics linearization; Eq. (6) can be linearized around a reference trajectory and control $\{\mathbf{x}^*(t), \mathbf{u}^*(t)\}$ based on a first-order truncation of the Taylor expansion:

$$d\mathbf{x} \approx [A(t)\mathbf{x} + B(t)\mathbf{u} + \mathbf{c}(t)] dt + G(t) d\mathbf{w} \quad (21)$$

*For simplicity, in this work, we assume that the control discretization intervals are the same as the filter update intervals. It is straightforward to extend the formulation to cases where the interval lengths are integer multiples of each other; for example, requiring that the control between two nodes are constant can be imposed as a simple linear equality constraint.

where

$$A = \left. \frac{\partial \mathbf{f}}{\partial \mathbf{x}} \right|_{\mathbf{x}^*, \mathbf{u}^*}, \quad B = \left. \frac{\partial \mathbf{f}}{\partial \mathbf{u}} \right|_{\mathbf{x}^*, \mathbf{u}^*}, \quad \mathbf{c} = \mathbf{f}(\mathbf{x}^*, \mathbf{u}^*) - A\mathbf{x}^* - B\mathbf{u}^*, \quad G = \mathbf{g}(\mathbf{x}^*, \mathbf{u}^*) \quad (22)$$

With the zero-order hold control assumption, we can exactly discretize the linearized dynamics as

$$\mathbf{x}_{k+1} = A_k \mathbf{x}_k + B_k \mathbf{u}_k + \mathbf{c}_k + G_k \mathbf{w}_k, \quad k = 0, \dots, N-1 \quad (23)$$

where the discrete-time matrices can be evaluated by simultaneous numerical integration of the following ordinary differential equations from time t_k to t_{k+1} [27, 28]:

$$\frac{d}{dt} \mathbf{x}(t) = \mathbf{f}(\mathbf{x}(t), \mathbf{u}_k^*), \quad \mathbf{x}(t_k) = \mathbf{x}_k^* \quad (24a)$$

$$\frac{d}{dt} \Phi_A(t, t_k) = A(t) \Phi_A(t, t_k), \quad \Phi_A(t_k, t_k) = I_{n_x} \quad (24b)$$

$$\frac{d}{dt} \Phi_B(t, t_k) = A(t) \Phi_B(t, t_k) + B(t), \quad \Phi_B(t_k, t_k) = \mathbf{0}_{n_x \times n_u} \quad (24c)$$

$$\frac{d}{dt} \Phi_P(t, t_k) = A(t) \Phi_P(t, t_k) + \Phi_P(t, t_k) A(t)^T + G(t) G(t)^T, \quad \Phi_P(t_k, t_k) = \mathbf{0}_{n_x \times n_x} \quad (24d)$$

Letting $\bar{\boldsymbol{\phi}}(t_{k+1})$ be the result of integrating Eq. (24a) from t_k to t_{k+1} ,

$$A_k = \Phi_A(t_{k+1}, t_k), \quad B_k = \Phi_B(t_{k+1}, t_k), \quad \mathbf{c}_k = \bar{\boldsymbol{\phi}}(t_{k+1}) - A_k \mathbf{x}_k^* - B_k \mathbf{u}_k^* \quad (25)$$

and G_k is any matrix that satisfies $G_k G_k^T = \Phi_P(t_{k+1}, t_k)$. Note that when the reference state and control are known at each time step, the computation of the discrete matrices for each segment is independent and can be parallelized.

C. Filtered Discrete Covariance Propagation

Having derived the linearized covariance propagation model, we assume that the filtering process is a Kalman filter, since the Kalman filter is a minimum-variance estimator for linear systems with Gaussian noise [28]. The nonlinear observation process Eq. (10) can also be linearized with respect to a reference state, as

$$\mathbf{y}_k = C_k \mathbf{x}_k + D_k \mathbf{v}_k + \mathbf{c}_{\text{obs},k} \quad (26)$$

where

$$C_k = \left. \frac{\partial \mathbf{f}_{\text{obs}}}{\partial \mathbf{x}} \right|_{\mathbf{x}_k^*}, \quad D_k = \mathbf{g}_{\text{obs}}(\mathbf{x}_k^*), \quad \mathbf{c}_{\text{obs}} = \mathbf{f}_{\text{obs}}(\mathbf{x}_k^*) - C_k \mathbf{x}_k^* \quad (27)$$

Between each time step, the Kalman filter updates the state estimate

$$\hat{\mathbf{x}}_k^- = A_{k-1} \hat{\mathbf{x}}_{k-1} + B_{k-1} \mathbf{u}_{k-1} + \mathbf{c}_{k-1} \quad (\text{time update}) \quad (28a)$$

$$\hat{\mathbf{x}}_k = \hat{\mathbf{x}}_k^- + L_k \tilde{\mathbf{y}}_k^- \quad (\text{measurement update}) \quad (28b)$$

where \mathbf{x}_k^- is the apriori estimated state, $\hat{\mathbf{x}}_k$ is the estimated state, and innovation process $\tilde{\mathbf{y}}_k^-$ is defined as

$$\tilde{\mathbf{y}}_k^- = \mathbf{y}_k - (\mathbf{c}_{\text{obs},k} + C_k \hat{\mathbf{x}}_k^-) \quad (29)$$

L_k is the Kalman gain,

$$L_k = \tilde{P}_k^- C_k^\top (C_k \tilde{P}_k^- C_k^\top + D_k D_k^\top)^{-1} \quad (30)$$

where $\tilde{P}_k^- := \text{Cov}[\mathbf{x}_{k-}]$ is the apriori estimated state covariance. The Kalman gain can be analytically calculated *pre-optimization* from \tilde{P}_k^- and $\tilde{P}_k := \text{Cov}[\tilde{\mathbf{x}}_k]$, the estimation error covariance [28]:

$$\tilde{P}_k^- = A_{k-1} \tilde{P}_{k-1} A_{k-1}^\top + G_{\text{exe},k-1} G_{\text{exe},k-1}^\top + G_{k-1} G_{k-1}^\top \quad (31a)$$

$$\tilde{P}_k = (I - L_k C_k) \tilde{P}_k^- (I - L_k C_k)^\top + L_k D_k D_k^\top L_k^\top \quad (31b)$$

The innovation process is Gaussian-distributed with zero mean and covariance

$$P_{\tilde{\mathbf{y}}_k^-} = C_k \tilde{P}_k^- C_k^\top + D_k D_k^\top \quad (32)$$

Combining Eq. (28), we get the discrete dynamics of the state estimate:

$$\hat{\mathbf{x}}_{k+1} = A_k \hat{\mathbf{x}}_k + B_k \mathbf{u}_k + \mathbf{c}_k + L_{k+1} \tilde{\mathbf{y}}_{k+1}^-, \quad \hat{\mathbf{x}}_0 = L_0 \tilde{\mathbf{y}}_0^- \quad (33)$$

Substituting the affine TCM policy Eq. (20) into the belief space dynamics, we get

$$\hat{\mathbf{x}}_{k+1} = (A_k + B_k K_k) \hat{\mathbf{x}}_k + B_k \bar{\mathbf{u}}_k + \mathbf{c}_k + L_{k+1} \tilde{\mathbf{y}}_{k+1}^- \quad (34)$$

and its mean and covariance dynamics can be derived as

$$\bar{\mathbf{x}}_{k+1} = A_k \bar{\mathbf{x}}_k + B_k \bar{\mathbf{u}}_k + \mathbf{c}_k, \quad \bar{\mathbf{x}}_0 = \boldsymbol{\mu}_0 \quad (35a)$$

$$\hat{P}_{k+1} = (A_k + B_k K_k) \hat{P}_k (A_k + B_k K_k)^\top + \hat{Q}_{k+1}, \quad \hat{P}_0 = \hat{P}_0^- + \hat{Q}_0 \quad (35b)$$

where $\bar{\mathbf{x}}_k$ and \hat{P}_k are the mean and covariance of the state estimate, respectively and define for simplicity, $\hat{Q}_k := L_k P_{\tilde{\mathbf{y}}_k^-} L_k^\top$. [13] shows that the state covariance can be obtained by simply adding the covariance of the state estimate

and the estimation error:

$$P_k := \text{Cov}[\mathbf{x}_k] = \tilde{P}_k + \hat{P}_k \quad (36)$$

The developments in this section allow us to write Problem 1 as follows. Note that while the linearized dynamics and the Kalman filter are used to approximate the covariance propagation, the mean of the state estimate is propagated through the nonlinear dynamics, as is done for the EKF. For the problem to be well-defined as an optimization problem, and adhering to the spirit of the EKF, the linearized system matrices $A_k, B_k, \mathbf{c}_k, \hat{Q}_k$ should be written as functions of the state estimate mean $\bar{\mathbf{x}}_k$. For now, we assume that the linearization is performed around a given reference trajectory.

Problem 2 *Discretized Chance-Constrained ΔV_{99} Minimization with Belief-Space Mean/Covariance Propagation*

$$\text{minimize } Q\left(\sum_{k=0}^{N-1} \|\mathbf{u}_k\|; 0.99\right) \quad (37a)$$

$$\text{s.t. } \bar{\mathbf{x}}_{k+1} = \bar{\mathbf{x}}_k + \int_{t_k}^{t_{k+1}} \mathbf{f}(\bar{\mathbf{x}}, \bar{\mathbf{u}}_k, t) dt \quad (37b)$$

$$\hat{P}_{k+1} = (A_k + B_k K_k) \hat{P}_k (A_k + B_k K_k)^\top + \hat{Q}_{k+1} \quad (37c)$$

$$\mathbb{P}[\|\mathbf{u}_k\| \leq u_{\max}] \geq 1 - \epsilon_u \quad (37d)$$

$$\hat{P}_k + \tilde{P}_k \leq P_{\max} \quad (37e)$$

$$\bar{\mathbf{x}}_N = \boldsymbol{\mu}_f, \quad \hat{P}_N + \tilde{P}_N \leq P_f \quad (37f)$$

IV. Solution via Convexification and Sequential Convex Programming

In this section, we present a numerical solution method to Problem 2. The cost function and chance constraints are reformulated as deterministic second-order cone expressions, and the covariance dynamics are reformulated as affine equality constraints via lossless convexification. This allows us to solve the problem via sequential convex programming.

A. Deterministic Convex Formulation

1. Objective Function Upper Bound

To reformulate the optimization problem as a tractable deterministic optimization, we first provide a deterministic upper bound on the objective function. Under the linear covariance propagation and Gaussian initial state estimate distribution, each control input is Gaussian-distributed and its mean and covariance are given by

$$\mathbb{E}[\mathbf{u}_k] = \bar{\mathbf{u}}_k, \quad \text{Cov}[\mathbf{u}_k] = K_k \hat{P}_k K_k^\top \quad (38)$$

Hence, our objective function is a sum of the Euclidean norms of Gaussian-distributed random variables. To the authors' knowledge, there is no closed-form expression (in terms of the variable's mean and covariance) for the quantile function

of the Euclidean norm of a nonzero-mean Gaussian random variable. However, we can provide a deterministic upper bound; using the triangle inequality, [16] provides the following bound:

$$Q(\|\mathbf{u}_k\|; p) \leq \|\mathbb{E}[\mathbf{u}_k]\| + \sqrt{Q_{\chi_{n_u}^2}(p)} \sqrt{\lambda_{\max}(\text{Cov}[\mathbf{u}_k])} := \tilde{Q}(\|\mathbf{u}_k\|; p) \quad (39)$$

where $Q_{\chi_{n_u}^2}(\cdot)$ is the inverse cumulative distribution function for a chi-squared distribution with n_u degrees of freedom. In later simulations, we see that this bound is quite tight for the problem settings we consider. Notice that the objective function is now separated into a sum of a term involving the mean dynamics and a term involving the covariance dynamics, which we can write as J_μ and J_Σ .

2. Case with No Chance Constraints

In the absence of chance constraints, the mean steering problem and covariance steering problem are decoupled [18]. Hence, we can solve two separate optimization problems:

Problem 3 (Mean steering problem) minimize J_μ subject to the filtered mean dynamics Eq. (35a) with mean terminal constraint of Eq. (16).

Problem 4 (Covariance steering problem) minimize J_Σ subject to the filtered covariance dynamics Eq. (35b) with covariance terminal constraint of Eq. (16).

While the mean steering problem is a traditional nonlinear trajectory optimization problem for which various solution methods exist, the covariance steering problem involves an equality that is cubic in the variables \hat{P}_k and K_k . However, [18, 19] show that we can equivalently formulate the problem as a convex optimization for a certain class of objective functions, by utilizing *lossless convexification*, i.e. the solution obtained from solving a convex optimization problem gives the solution for the original nonconvex problem. The procedure for lossless convexification is as follows: 1. replace K_k by a set of new decision variables $U_k \in \mathbb{R}^{n_u \times n_x}$ such that $U_k := K_k \hat{P}_k$, 2. introduce additional decision variables $Y_k \in \mathbb{R}^{n_u \times n_u}$, 3. rewrite the covariance equations with U_k , replacing the expression $U_k \hat{P}_k^{-1} U_k^\top$ that appears, with Y_k , 4. additionally impose the linear matrix inequality (LMI) constraint

$$\begin{bmatrix} \hat{P}_k & U_k^\top \\ U_k & Y_k \end{bmatrix} \geq 0 \quad (40)$$

Then, the covariance steering problem is equivalently formulated as

$$\underset{Y_k, U_k, \hat{P}_k}{\text{minimize}} \quad J_\Sigma \quad (41a)$$

$$\text{s.t. } \hat{P}_{k+1} = A_k \hat{P}_k A_k^\top + B_k U_k A_k^\top + A_k U_k^\top B_k^\top + B_k Y_k B_k^\top + \hat{Q}_{k+1} \quad (41b)$$

$$\begin{bmatrix} \hat{P}_k & U_k^\top \\ U_k & Y_k \end{bmatrix} \geq 0 \quad (41c)$$

$$\hat{P}_0 = \hat{P}_{0^-} + \hat{Q}_0, \quad P_f - \hat{P}_N - \tilde{P}_N \geq 0 \quad (41d)$$

The feedback gains can be retrieved post-optimization by $K_k = U_k \hat{P}_k^{-1}$, and Y_k represents the control covariance matrix at optimality. [18, 19] prove the validity of the lossless convexification for objectives with expectation-of-quadratic cost; essentially, the proof for lossless convexification relies on the objective function satisfying

$$\frac{\partial J_\Sigma}{\partial Y_k} > 0 \quad (42)$$

which is true for the expectation-of-quadratic case. Unfortunately, for quantile 2-norm minimization, since [29]

$$\frac{\partial \sqrt{\lambda_{\max}(Y_k)}}{\partial Y_k} = \frac{1}{2\sqrt{\lambda_{\max}(Y_k)}} \frac{\partial \lambda_{\max}(Y_k)}{\partial Y_k} = \frac{1}{2\sqrt{\lambda_{\max}(Y_k)}} \mathbf{v}_{\max} \mathbf{v}_{\max}^\top \quad (43)$$

where \mathbf{v}_{\max} is the eigenvector corresponding to the maximum eigenvalue $\lambda_{\max}(Y_k)$, this cost function only satisfies $\frac{\partial \sqrt{\lambda_{\max}(Y_k)}}{\partial Y_k} \geq 0$ (not strict linear matrix inequality), hence we cannot guarantee lossless convexification. Thus, we add an additional term in the objective:

$$J_\Sigma := \sum_k \sqrt{Q_{\chi_{nu}^2}(p)} \sqrt{\lambda_{\max}(Y_k)} + \epsilon_Y \text{tr}(Y_k) \quad (44)$$

where $\epsilon_Y > 0$ is a small scalar to be chosen by the user. Since $\partial \text{tr}(Y_k)/\partial Y_k = I > 0$, adding this term guarantees that Eq. (42) is satisfied, hence the convexification is lossless.

3. Chance-Constrained Problem

When chance constraints are present, the mean and covariance are coupled in the constraints. Here, we focus on the 2-norm upper bound on the control input. With the same derivation as for the objective function, we can formulate a conservative deterministic form as

$$\|\bar{\mathbf{u}}_k\| + \sqrt{Q_{\chi_{nu}^2}(1 - \epsilon_u)} \sqrt{\lambda_{\max}(Y_k)} \leq u_{\max} \quad (45)$$

since we already introduced the decision variable Y_k which will be equal to the covariance of the control at optimality, i.e. $Y_k = K_k \hat{P}_k K_k^\top$. $\lambda_{\max}(\cdot)$ is a convex operator for symmetric matrices [30]. However, the square root over the

maximum eigenvalue operator makes this deterministic formulation nonconvex. In order to handle this nonconvexity in the framework of SCP, we decompose this constraint into two inequalities, one of which remains nonconvex. The nonconvexity is treated via slack variables and Augmented Lagrangian penalization in the objective function, which is a method with proven guarantees on optimality. We introduce a set of variables $\tau_{0:N-1} \geq 0$, such that

$$\lambda_{\max}(Y_k) - \tau_k^2 \leq 0 \quad (46)$$

Then, Eq. (45) is implied by the second-order cone constraint:

$$\|\bar{\mathbf{u}}_k\| + \sqrt{\mathbf{Q}_{\chi_{n_u}^2}(p)} \cdot \tau_k \leq u_{\max} \quad (47)$$

Although Eq. (46) is a difference-of-convex form and thus nonconvex, we simply linearize the concave term around some reference for τ , which we denote as τ^{ref} :

$$\lambda_{\max}(Y_k) - (\tau_k^{\text{ref}})^2 - 2\tau_k^{\text{ref}}(\tau_k - \tau_k^{\text{ref}}) \leq \zeta_k \quad (48)$$

where $\zeta_k \geq 0$ is a slack variable, which is penalized in the objective function via the SCvx* framework if it takes positive values.

Remark 2 (Conservativeness of the control upper bound relaxation) *Eq. (46) is not guaranteed to be satisfied with equality, hence this is a potentially conservative approximation to Eq. (45) (which is already a conservative approximation of Eq. (14a)). However, this method has performed most reliably and predictably compared to globally overapproximating the square root via its linearization [31] or exactly imposing difference-of-convex forms without slack variables[19]. The numerical simulations also show little conservativeness in the control profile.*

We finally show the subproblem that is solved at each iteration of the SCP algorithm. The objective function is a second-order-cone expression; the constraints are either linear matrix inequalities, second-order cone constraints, or affine equalities, since ∞ -norm constraints can be written as affine inequalities via auxiliary variables, and $\lambda_{\max}(\cdot)$ inequalities can be written as LMIs. Hence, the subproblem is a semidefinite programming (SDP), which can be solved via off-the-shelf solvers such as MOSEK [32]. For simplicity, we do not show the reformulation of these constraints into standard SDP form, since parsers such as YALMIP [33] automate this process; see also [30] for details. The slack variables are penalized in the objective function via a function $J_{\text{pen}}(\cdot)$. For notational simplicity, define $\mathbf{z} := \{\bar{\mathbf{x}}_{0:N}, \hat{P}_{0:N}, \bar{\mathbf{u}}_{0:N-1}, U_{0:N-1}, Y_{0:N-1}, \tau_{0:N-1}\}$, $\boldsymbol{\xi} := [\boldsymbol{\xi}_0^T, \dots, \boldsymbol{\xi}_{N-1}^T]^T$, $\boldsymbol{\zeta} := [\zeta_0, \dots, \zeta_{N-1}]^T$, and

$$J_0(\mathbf{z}) := \sum_{k=0}^{N-1} \|\bar{\mathbf{u}}_k\| + \sqrt{\mathbf{Q}_{\chi_{n_u}^2}(0.99)} \cdot \tau_k + \epsilon_Y \text{tr}(Y_k) \quad (49)$$

Problem 5 (SDP subproblem solved at each SCP Iteration)

$$\underset{z, \xi, \zeta \geq 0}{\text{minimize}} \quad J_{\text{aug}}(z, \xi, \zeta) := J_0(z) + J_{\text{pen}}(\xi, \zeta) \quad (50a)$$

$$\text{s.t.} \quad \bar{\mathbf{x}}_{k+1} - (A_k \bar{\mathbf{x}}_k + B_k \bar{\mathbf{u}}_k + \mathbf{c}_k) + \xi_k = 0 \quad k = 0, \dots, N-1 \quad (50b)$$

$$\hat{P}_{k+1} = A_k \hat{P}_k A_k^\top + B_k U_k A_k^\top + A_k U_k^\top B_k^\top + B_k Y_k B_k^\top + \hat{Q}_{k+1} \quad k = 0, \dots, N-1 \quad (50c)$$

$$\begin{bmatrix} \hat{P}_k & U_k^\top \\ U_k & Y_k \end{bmatrix} \geq 0 \quad k = 0, \dots, N-1 \quad (50d)$$

$$\lambda_{\max}(Y_k) - (\tau_k^{\text{ref}})^2 - 2\tau_k^{\text{ref}}(\tau_k - \tau_k^{\text{ref}}) \leq \zeta_k \quad k = 0, \dots, N-1 \quad (50e)$$

$$\|\bar{\mathbf{u}}_k\| + \sqrt{Q_{\lambda_{nu}}^2 (1 - \epsilon_u)} \cdot \tau_k - u_{\max} \leq 0 \quad k = 0, \dots, N-1 \quad (50f)$$

$$\hat{P}_k + \tilde{P}_k \leq P_{\max} \quad k = 0, \dots, N \quad (50g)$$

$$\bar{\mathbf{x}}_0 = \boldsymbol{\mu}_0, \quad \bar{\mathbf{x}}_N = \boldsymbol{\mu}_N, \quad \hat{P}_0 = \hat{P}_0^- + \hat{Q}_0, \quad P_f - \hat{P}_N - \tilde{P}_N \geq 0 \quad (50h)$$

$$\hat{P}_k \in \mathbb{S}^{n_x} \quad k = 0, \dots, N \quad (50i)$$

$$Y_k \in \mathbb{S}^{n_u}, Y_k \geq 0, \tau_k \geq 0 \quad k = 0, \dots, N-1 \quad (50j)$$

$$s_{\bar{\mathbf{x}}}\|\bar{\mathbf{X}} - \bar{\mathbf{X}}^{\text{ref}}\|_{\infty} \leq \Delta_{\text{TR}}, \quad s_{\bar{\mathbf{u}}}\|\bar{\mathbf{U}} - \bar{\mathbf{U}}^{\text{ref}}\|_{\infty} \leq \Delta_{\text{TR}}, \quad s_{\tau}\|\boldsymbol{\tau} - \boldsymbol{\tau}^{\text{ref}}\|_{\infty} \leq \Delta_{\text{TR}} \quad (50k)$$

While the initial reference trajectory for obtaining the linearized dynamics can be obtained by solving the deterministic version of the problem through some trajectory optimization algorithm, an initial reference $\tau_{0:N-1}^{\text{ref}}$ is also required to initialize the SCP algorithm. This can be obtained by solving the covariance steering problem with $\sum \text{tr}(Y_k)$ cost, where the linear system matrices are obtained by linearization around the initial reference trajectory. Then, we can set $\tau_k^{\text{ref}} = \sqrt{\lambda_{\max}(Y_k)}$ for each k .

Eq. (50k) imposes trust region constraints to maintain the validity of the linearization by restricting the variation from the linearization reference to be sufficiently small. Δ_{TR} is the trust region, which is updated according to the algorithm's framework. Since the scaling of variables are different, we use a different scaling for the trust region, in the form of $s_{(\cdot)}$ is the scaling value for each variable. $\bar{\mathbf{X}} := [\bar{\mathbf{x}}_0^\top, \bar{\mathbf{x}}_1^\top, \dots, \bar{\mathbf{x}}_N^\top]^\top$, and similarly for other variables. The ref superscript denotes the reference value, which is the value of the variable at a previous iteration. We choose $s_{\bar{\mathbf{x}}} = 1$ and $s_{\bar{\mathbf{u}}} = u_{\max}$. s_{τ} is chosen based on the initial solve, set as $s_{\tau} = \max_k \tau_k$.

B. Sequential Convex Programming Scheme

We are ready to present the algorithm for the SCP-based CCDVO framework. The pseudoalgorithm is shown in Algorithm 1, based on the SCvx* algorithm [34]. z^{ref} is the reference solution from a previous iteration. Although we

Algorithm 1 Robust Trajectory Optimization under Uncertainty via SCvx*

Require: initial reference trajectory and control $\{\bar{\mathbf{X}}^{\text{ref}}, \bar{\mathbf{U}}^{\text{ref}}\}$

- 1: Solve covariance steering problem with trace objective to get initial reference values $\tau_{0:N-1}^{\text{ref}}$
- 2: **while** iterations don't exceed the maximum **do**
- 3: **if** first iteration or the reference was updated in previous iteration **then**
- 4: \lfloor Compute $\{A_k, B_k, \mathbf{c}_k, \hat{Q}_k, \tilde{P}_k\}$ from $\{\bar{\mathbf{X}}^{\text{ref}}, \bar{\mathbf{U}}^{\text{ref}}\}$
- 5: $\mathbf{z} \leftarrow$ solve Problem 5
- 6: **if** convergence criteria met **then** \triangleright Line 2 of [34]
- 7: **return** \mathbf{z}
- 8: **if** acceptance conditions met **then** \triangleright Eq. (55)
- 9: $\mathbf{z}^{\text{ref}} \leftarrow \mathbf{z}$ \triangleright solution update
- 10: Update penalty weight w , Lagrange multipliers λ, μ \triangleright Line 13-15, Algorithm 1 of [34]
- 11: Update trust region Δ_{TR} \triangleright Eq. (56)

use the algorithm almost unchanged from the reference, there are a few aspects that warrant some discussion, including small algorithmic modifications to extend the algorithm to be applicable to trajectory optimization under uncertainty. These aspects are highlighted in the following. Readers are referred to the reference for further details on the algorithm.

1. Augmented Lagrangian Penalty Function

One notable difference is the augmented penalty in the objective function; we use the form

$$J_{\text{pen}}(\xi, \zeta; w, \lambda, \mu) = \mu \cdot \xi + \frac{w}{2} \xi \cdot \xi + \sqrt{w} \|\xi\|_1 + \lambda \cdot \zeta + \frac{w}{2} \max(0, \zeta) \cdot \max(0, \zeta) + \sqrt{w} \|\max(0, \zeta)\|_1 \quad (51)$$

where μ, λ are the Augmented Lagrangian multipliers for the equality and inequality constraints, respectively, and w is the penalty weight. Note that ξ and ζ are not limited to our earlier definitions, but can be generalized to any equality/inequality slack variables. In contrast to the original SCvx* penalty, the penalty function additionally penalizes the 1-norm of the constraint violation; as also noted in [35], adding this additional term empirically results in convergence with fewer iterations.

2. Step Acceptance and Trust Region Update

A key step in Algorithm 1 is determining *solution acceptance* in line 8. Like in [34, 36], the condition for solution acceptance is based on the ratio of the nonlinear cost reduction ΔJ to the approximated cost reduction ΔL , as follows:

$$\rho = \frac{\Delta J}{\Delta L} = \frac{J_{\text{aug}}^{\text{NL}}(\mathbf{z}^{\text{ref}}) - J_{\text{aug}}^{\text{NL}}(\mathbf{z}^*)}{J_{\text{aug}}^{\text{NL}}(\mathbf{z}^{\text{ref}}) - J_{\text{aug}}(\mathbf{z}^*, \xi^*, \zeta^*)} \quad (52)$$

where J_{aug} is given in Eq. (50a) while $J_{\text{aug}}^{\text{NL}}$ represents the cost of the nonlinear “original” problem with augmented Lagrangian,

$$J_{\text{aug}}^{\text{NL}}(\mathbf{z}) := J_0(\mathbf{z}) + J_{\text{pen}}(\mathbf{g}(\mathbf{z}), \mathbf{h}(\mathbf{z}); w, \lambda, \mu) \quad (53)$$

with \mathbf{g} , \mathbf{h} being the original nonconvex expressions for the equality/inequality constraints which are linearized in the subproblem, in this case,

$$\mathbf{g}(\mathbf{z}) = \begin{bmatrix} \bar{\mathbf{x}}_1 - \left(\bar{\mathbf{x}}_0 + \int_{t_0}^{t_1} \mathbf{f}(\bar{\mathbf{x}}, \bar{\mathbf{u}}_0, t) dt \right) \\ \vdots \\ \bar{\mathbf{x}}_N - \left(\bar{\mathbf{x}}_{N-1} + \int_{t_{N-1}}^{t_N} \mathbf{f}(\bar{\mathbf{x}}, \bar{\mathbf{u}}_{N-1}, t) dt \right) \end{bmatrix}, \quad \mathbf{h}(\mathbf{z}) = \begin{bmatrix} \lambda_{\max}(Y_0) - \tau_0^2 \\ \vdots \\ \lambda_{\max}(Y_{N-1}) - \tau_{N-1}^2 \end{bmatrix} \quad (54)$$

Note the same values of ω , λ , μ are used when calculating all the $J_{\text{aug}}^{\text{NL}}$ and J_{aug} in Eq. (52).

The value of ρ is then used to determine whether to accept the current iteration and how to update the trust region radius Δ_{TR} . In this work, we employ a different scheme than the one proposed in [34]. For $1 \geq \eta_0 > \eta_1 > \eta_2 > 0$, the step acceptance criterion is defined as:

$$\begin{cases} \text{accept} & \text{if } \rho \in [1 - \eta_0, 1 + \eta_0] \\ \text{reject} & \text{else} \end{cases} \quad (55)$$

while the trust region is updated as follows:

$$\Delta_{\text{TR}} \leftarrow \begin{cases} \max \{ \alpha_2 \Delta_{\text{TR}}, \Delta_{\text{TR}, \min} \} & \text{if } \rho \in [1 - \eta_2, 1 + \eta_2] \\ \Delta_{\text{TR}} & \text{elseif } \rho \in [1 - \eta_1, 1 + \eta_1] \\ \min \{ \Delta_{\text{TR}} / \alpha_1, \Delta_{\text{TR}, \max} \} & \text{else} \end{cases} \quad (56)$$

where $\alpha_1 > 1$ and $\alpha_2 > 1$ determine the contracting and enlarging ratios of Δ_{TR} , respectively, and $0 < \Delta_{\text{TR}, \min} < \Delta_{\text{TR}, \max}$ are the lower and upper bounds of the trust region radius.

This reformulation of the acceptance criterion and trust region update scheme is motivated by the fact that the convex subproblem presented in Problem 2, and hence Problem 5, is based on *inexact linearization* of the state covariance propagation (see Remark 3). This inexactness affects the analysis in the proof of Lemma 3 of [34], allowing ΔL defined in Eq. (52) to take negative values (Lemma 3 of [34] proves $\Delta L \geq 0$ assuming exact linearization). This observation implies that, under inexact linearization, a solution to the convex subproblem may yield $\Delta L < 0$, and that a solution with $\Delta J < 0$ is certainly a valid step as long as $\Delta L \approx \Delta J$. Thus, this work proposes the criterion given in Eq. (55) to accept a solution whenever ρ is close to unity, which happens when the nonlinear and linear cost reductions take similar values. This algorithmic choice is in a similar spirit to a successful trajectory optimization algorithm, hybrid differential dynamic programming (HDDP) [37], which applies augmented Lagrangian framework to DDP.

Another implication of inexact linearization is that Algorithm 1 does not fully inherit the convergence guarantee

provided by the SCvx* algorithm. The convergence guarantee of the original SCvx* algorithm relies on the non-negativity of ΔL , which, again, is not guaranteed here. Note that this inexact linearization issue is present in other formulations for SCP-based trajectory optimization under uncertainty (e.g., [13–15, 38]), although none of these studies seem to have pointed out this fact. Rigorously analyzing the convergence behavior of SCP algorithms under inexact linearization, especially those for trajectory optimization under uncertainty, is left for important future work.

Remark 3 *The linearized filtered state covariance dynamics given by Eq. (37c) do not provide exact linearization of the state covariance propagation of the original system given in Eq. (6). As apparent in Eq. (37c), propagation of $P_k (= \hat{P}_k + \tilde{P}_k)$ depends on the evaluation of the matrices A_k, B_k, c_k, \hat{Q}_k , etc, which are obtained by linearizing the system about the reference mean $\{\bar{X}^{\text{ref}}, \bar{U}^{\text{ref}}\}$. On the other hand, the current formulation in Eq. (37c) does not capture the effect of changes in the mean trajectory $\{\bar{X}, \bar{U}\}$ to those in A_k, B_k, c_k, \hat{Q}_k , etc, resulting in inexact linearization. To exactly linearize the problem with respect to variables, one needs to capture the effect of change in $\{\bar{X}, \bar{U}\}$, which however requires the second-order sensitivity, i.e., state transition tensor (STT). Although using STTs would address the inexact linearization issue, it would require a significantly heavier computational effort, for likely marginal improvement of the overall SCP performance.*

C. Scaling System Matrices and Variables to Resolve Numerical Issues

An issue inherent in space trajectory optimization problems is that the dispersion of the variables is much smaller than the value of the mean. If we solve the above problem without scaling, off-the-shelf solvers struggle with numerical issues, resulting in either warnings by the solver and/or constraints being violated with unignorable numerical errors. Thus, it is necessary to introduce scaling of the constraints relating to the covariance. Although it is difficult to entirely resolve bad scaling in all constraint coefficients and variables, and most off-the-shelf solvers apply their own internal scaling scheme to mediate numerical issues, scaling strategies are still important in avoiding the aforementioned issues.

1. Proposed Scaling Method

The scaling strategy is quite simple: introduce a scalar $d > 1$ and substitute the variables that relate to the covariance \hat{P}_k, U_k, Y_k , with $\hat{P}_k \leftarrow d^2 \cdot \hat{P}_k, U_k \leftarrow d^2 \cdot U_k$, and so on. One can see that the covariance dynamics equation Eq. (50c) remains the same, but with the coefficients $\hat{Q}_k, P_{\max}, P_f, \tilde{P}_k$ replaced with $d^2 \cdot \hat{Q}_k, d^2 \cdot P_{\max}$, and so on. The linear matrix inequality Eq. (50d) remains the same since the LHS is multiplied by a positive scalar. The result of this scaling results in a ill-scaled reformulation for the objective and chance constraints, the objective function without penalty function augmentation becomes

$$\sum_{k=0}^{N-1} \|\bar{u}_k\| + \sqrt{Q_{\chi_{nu}^2}(0.99)} \cdot \tau_k/d + \epsilon_Y \text{tr}(Y_k)/d^2 \quad (57)$$

Note that τ_k is replaced with $d \cdot \tau_k$, from Eq. (46), so it is divided by d . We can similarly rescale the chance constraint. Although the objective and chance constraints become ill-scaled, this did not cause noticeable numerical issues. After solving the optimization, the variables in the original scaling can be recovered by reversing the scaling. Another benefit of introducing the scaling is that the use of slack variables in the linearized constraints will be similarly penalized, leading to faster reduction of the slack variable values.

2. Comparison with a Different Scaling Method

In our previous paper [38], we implemented another scaling scheme based on [14]. Choosing a scaling matrix $D \in \mathbb{R}^{n_x \times n_x}$, both the coefficients of the covariance dynamics and the variables were scaled as follows:

$$A_k \leftarrow DA_kD^{-1}, \quad B_k \leftarrow DB_k, \quad \hat{Q}_k \leftarrow D\hat{Q}_kD^\top, \quad U_k \leftarrow U_kD, \quad \hat{P}_k \leftarrow D\hat{P}_kD^\top \quad (58)$$

However, we observed through further numerical experiments that this numerical scaling scheme is more prone to numerical issues compared to the above method. Our intuition for this is that the previous scheme introduces a wide range of scaling in the covariance-related variables, as U_k is scaled ‘up’ by D and \hat{P}_k is scaled ‘up’ by D^2 , while Y_k is not scaled at all, due to the D matrix canceling out in the losslessness-inducing LMI constraint. In addition, the coefficients of the covariance dynamics also possess a wide range of scaling, due to the quadratic term $B_kY_kB_k$ now being scaled ‘up’ by a factor D^2 while the term $A_k\hat{P}_kA_k^\top$ retains the same factor of scaling since $A_k \leftarrow DA_kD^{-1}$ approximately keeps the coefficient scaling. This wide range of scaling in the constraints and variables is likely the cause of the numerical issues.

Remark 4 (Comparisons between block Cholesky and full covariance formulations) *Compared to the block Cholesky type algorithms proposed in [13, 15], full covariance-type approaches, including our method, require significantly less computational effort. The former approaches construct a large linear matrix inequality (LMI) with size on the order of Nn_x -by- Nn_u , while the latter constructs N LMI’s on the order of $(n_x + n_u)$ -by- $(n_x + n_u)$ (see Eq. (50d)). Assuming that the main computational burden of solving the subproblem comes from the LMI’s, we can say that the computational complexity is $O(N^2n_xn_u)$ vs $O(N(n_x + n_u))$. As the number of discretization nodes increases, full covariance methods greatly outperform the block Cholesky methods. See also [19] for a comparison of solution times for the problem under linear dynamics (i.e. for the linearized subproblem). As noted later in the numerical results, our method for 200 discretization nodes requires ten minutes, while block Cholesky approaches would require several hours.*

Another advantage that full covariance approaches allows is the capability to perform feedback directly on the newest state estimate. While Eq. (20) seems to be a standard affine feedback policy, it has not been the norm for block Cholesky methods. such as state history feedback [13, 15] which requires storing all state histories and larger feedback gain matrices, and feedback based on a non-physical stochastic process [16, 39].

Remark 5 (Difference between ours and a similar method) While [14] proposes a similar full covariance approach, the lossless convexification proposed for the covariance propagation is lossy [17]. Although the numerical examples in [14] seem lossless, when implementing the algorithm for this work, we often encountered very lossy covariance propagations.

V. Numerical Simulations

Table 2 Uncertainty parameters for DRO–DRO (NRHO–Halo) transfer

Category	Error Type	Symbol	Value
Initial state estimate	Position std dev	$\tilde{\sigma}_{r_0^-}$	50 km
	Velocity std dev	$\tilde{\sigma}_{v_0^-}$	1 m/s
	Covariance matrix	\tilde{P}_{0^-}	$\text{blkdiag}(\tilde{\sigma}_{r_0^-}^2 I_3, \tilde{\sigma}_{v_0^-}^2 I_3)$
Final state	Position std dev	σ_{r_f}	20 km
	Velocity std dev	σ_{v_f}	0.1 m/s
	Covariance matrix	P_f	$\text{blkdiag}(\sigma_{r_f}^2 I_3, \sigma_{v_f}^2 I_3)$
Gates model	Fixed magnitude err std dev	σ_1	1 %
	Proportional magnitude error std dev	σ_2	0.5 deg
	Fixed pointing error std dev	σ_3	0.1 mm/s ²
	Proportional pointing error std dev	σ_4	0.1 mm/s ²
Navigation	Position std dev	σ_r^{nav}	10 km
	Velocity std dev	σ_v^{nav}	0.1 m/s
Chance constraints	Allowed control violation probability	ϵ_u	0.01
Maximum covariance	Position std dev	$\sigma_{r,\text{max}}$	∞ (500) km
	Velocity std dev	$\sigma_{v,\text{max}}$	∞ (3) m/s
	Covariance matrix	P_{max}	$\text{blkdiag}(\sigma_{r,\text{max}}^2 I_3, \sigma_{v,\text{max}}^2 I_3)$
Unmodeled acceleration	Stochastic acceleration	σ_a	$1 \times 10^{-10} (10^{-11}) \text{ km/s}^{3/2}$

This section demonstrates Algorithm 1 on two transfers between periodic orbits in the Earth-Moon CR3BP. The values of uncertainties for each scenario are shown in Table 2. The stochastic term in the SDE has a constant covariance matrix, with noise entering the state dynamics through change in velocity:

$$\mathbf{g}(\mathbf{x}, \mathbf{u}) = [0_{3 \times 3}, \sigma_a I_3]^\top$$

The orbit determination process is a full-state observation with Gaussian noise:

$$\mathbf{f}_{\text{obs}}(\mathbf{x}) = \mathbf{x}, \quad \mathbf{g}_{\text{obs}}(\mathbf{x}) = \text{blkdiag}(\sigma_r^{\text{nav}} I_3, \sigma_v^{\text{nav}} I_3)$$

The parameters for the SCvx* algorithm are shown in Table 3. The mass ratio is $\mu = 0.01215059$ for the CR3BP. Units for nondimensionalization are $\text{LU} = 384748 \text{ km}$ and $\text{TU} = 375700 \text{ s}$. $\epsilon_Y = 10^{-4}$ is used in Eq. (50a) and $d = 100$ for scaling. We use the ode78 propagator in MATLAB for all numerical integration, with absolute and relative tolerances

Table 3 SCvx* parameters

Parameter	$\{\epsilon_{\text{opt}}, \epsilon_{\text{feas}}\}$	$\{\eta_0, \eta_1, \eta_2\}$	$\{\alpha_1, \alpha_2\}$	β	γ	$\{\Delta_{\text{TR},\text{min}}, \Delta_{\text{TR},\text{max}}\}$	$\Delta_{\text{TR}}^{(1)}$	w_{max}	$w^{(1)}$
Value	$\{10^{-4}, 10^{-6}\}$	$\{1, 0.85, 0.1\}$	$\{2, 3\}$	2	0.9	$\{10^{-6}, 1\}$	0.3	10^8	1000

set to 10^{-13} . Convex optimization problems are solved with YALMIP [33] and MOSEK [32]. All simulations are performed with MATLAB on a standard personal laptop.

A. DRO–DRO Transfer

Table 4 Initial conditions for DROs ($y = z = \dot{x} = \dot{z} = 0$)

Orbit	x (ND)	\dot{y} (ND)	Period (ND)	Period (days)
DRO #1	0.58041127991124	0.973651613293327	5.71743682447432	≈ 25.3
DRO #2	0.233114246213419	2.41810511614024	6.2574913469559279	≈ 27.7

Table 5 Parameters for DRO-to-DRO transfer

Parameter	Value	Unit
Time-of-flight	25	days
Maximum s/c acceleration	0.5	mm/s ²
Discretization nodes	50	NA

As our first example, we consider a planar transfer between two Distant Retrograde Orbits (DROs), both around the L2 equilibrium. The initial conditions of the DROs are shown in Table 4. Depending on one’s working environment, differential corrections may be required to obtain a precisely closed orbit [25]. The problem parameters are summarized in Table 5. The initial reference trajectory is obtained as follows. First, the minimum-energy trajectory with unbounded control input is obtained with the indirect method, using the MATLAB nonlinear equation solver `fsolve`. With the implementation of the analytical derivatives of the shooting function (such as outlined in [40]), the indirect method with minimum-energy cost can be found easily, with initial random costate guesses. Next, the trajectory obtained is used as an initial reference trajectory in the sequential convex programming-based nonconvex optimization algorithm, SCvx* [34]. The generation of optimal reference trajectories is itself a vast topic, and we do not intend to claim that this is the best method; rather our focus is on ‘robustifying’ the nominal trajectories. The reference trajectory and control are shown in Fig. 2. The angles α, β are defined as $\alpha = \text{arctan2}(u_y/u_x)$ and $\beta = \arcsin\left(u_z/\sqrt{u_x^2 + u_y^2 + u_z^2}\right)$, with `arctan2` representing the four-quadrant inverse tangent function. Next, we apply Algorithm 1 to obtain optimal control policies to correct for operational and dynamics uncertainties. The algorithm converges in 6 iterations in 10 seconds. Note that this is orders of magnitude faster than the *block Cholesky* methods, which we have implemented in [15] and can require tens of minutes for convergence; this is consistent with the observations made in the linear covariance steering literature [19]. To verify our solution, we also perform a Monte Carlo simulation with 200 samples. Figs. 3 and 4 show the statistics

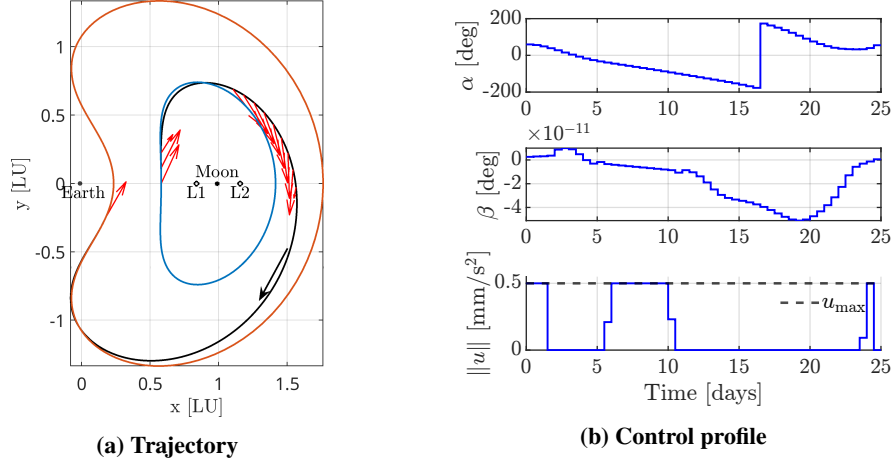


Fig. 2 Reference fuel-optimal DRO-to-DRO transfer from DRO #1 (inner) to DRO #2 (outer)

prediction based on the linear covariance model, as well as the Monte Carlo simulation results. The trajectories are shown in Fig. 3a, and the control profiles in Fig. 4. In Fig. 3a, the sample trajectories stay bounded throughout the

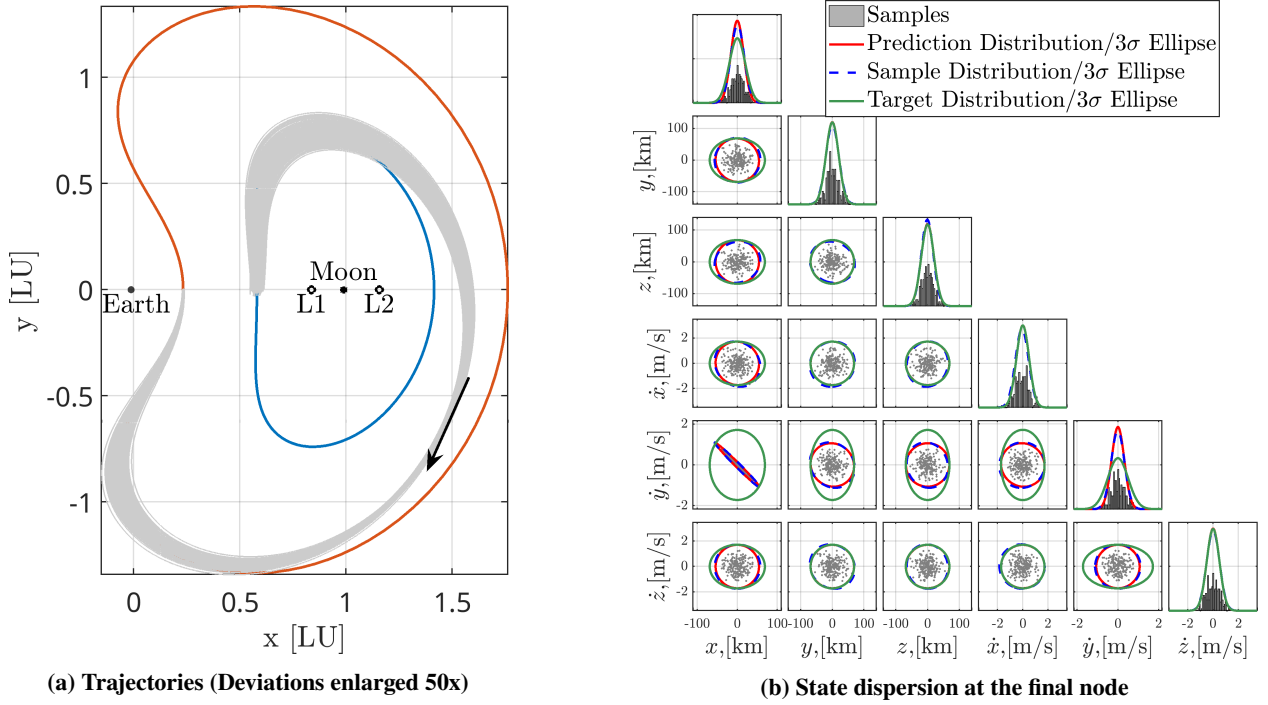


Fig. 3 Monte Carlo simulation trajectories for DRO-DRO transfer.

transfer thanks to the trajectory corrections, and the dispersion shrinks rapidly towards the end of the transfer. Figure 3b shows the statistics at the final epoch for each combination of the state variable, along with the distribution for the prediction ($P_N = \hat{P}_N + \tilde{P}_N$), samples, and target (P_f). The plots on the diagonals show the dispersions of each state component in terms of a histogram. We see that 1) the prediction distribution (red) accurately predicts the sample

distribution (blue) and 2) the sample distribution (blue) 3-sigma ellipses are within the target ellipse (green) in all state combinations, indicating that the final covariance constraint is satisfied in the Monte Carlo samples. Figure 4a shows

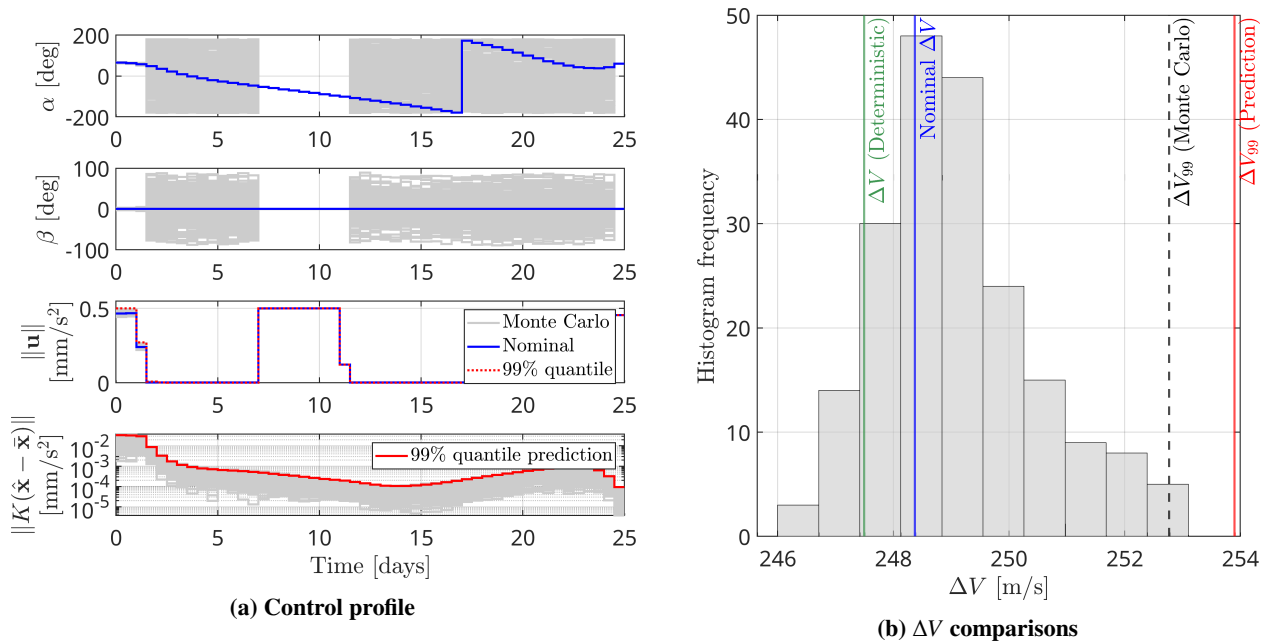


Fig. 4 Monte Carlo simulation control statistics for DRO-DRO transfer.

the control profile for the robust trajectories. The first two plots show the in-plane and out-of-plane control profiles for the nominal trajectory (blue) and the Monte carlo samples (grey). Comparing against the third plot, which shows the control acceleration magnitude, we see that during the thrusting arcs, the control is dominated by the feedforward term, resulting in small dispersion in the control angles. On the other hand, during the coasting arcs, the TC term dominates, resulting in larger dispersion in the control angles. The third plot also shows the 99% bound, computed from the left-hand side of Eq. (45). The bound accurately bounds the Monte Carlo samples, suggesting that the linear covariance model is also successful in predicting the control distribution. The fourth plot shows the control acceleration magnitude for the TC term only. We see that the TC effort is largest at the beginning of the transfer. There is also a smaller peak towards the end of the transfer, most likely in order to satisfy the final covariance constraint. Figure 4b shows the ΔV comparisons for the deterministic and robust trajectories. The deterministic trajectory has a lower ΔV compared to that of the nominal robust trajectory. We expect that this is due to the robust trajectory being optimized to also minimize the TC effort and the chance/distributional constraints. The ΔV_{99} prediction (red) successfully bounds that of the Monte Carlo samples (black broken line), suggesting that the ΔV_{99} prediction with our model can provide upper bounds for the Monte Carlo samples (without running the computationally expensive Monte Carlo simulation).

Table 6 Initial conditions for L2 NRHO to L1 Halo transfer. ($y = \dot{x} = \dot{z} = 0$)

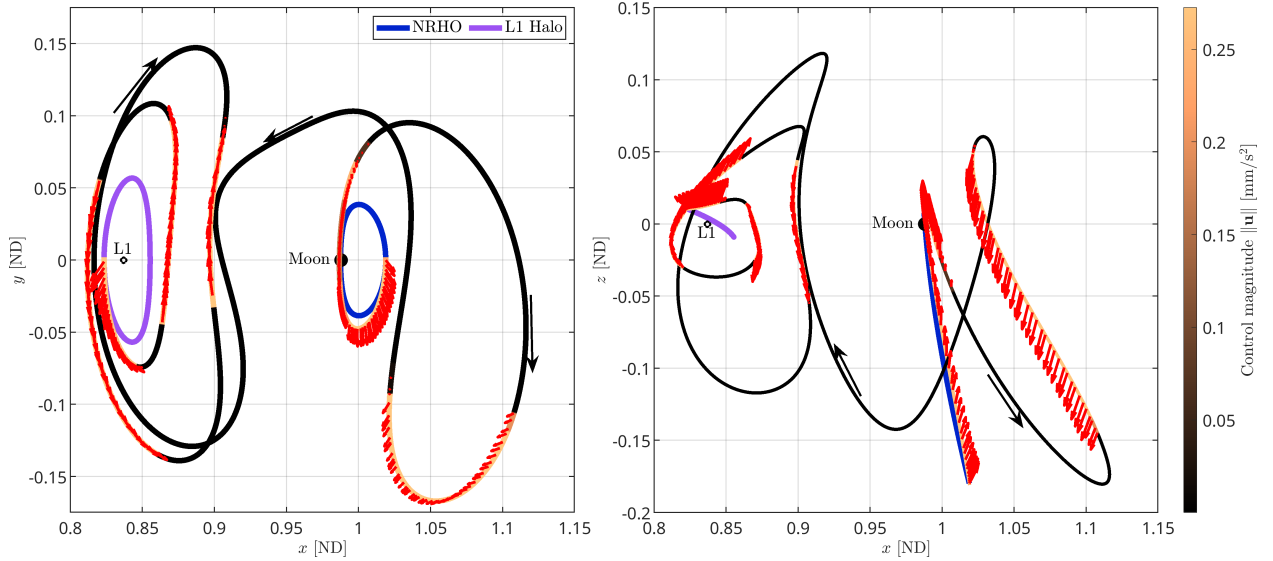
Orbit	x (ND)	z (ND)	\dot{y} (ND)	Period (days)
L2 NRHO	1.018826173554963	-0.179797844569828	-0.096189089845127	≈ 6.4
L1 Halo	0.823383959653906	0.010388134109586	0.128105259453086	≈ 12.0

Table 7 Parameters for L2 NRHO to L1 Halo transfer

Parameter	Value	Unit
Time-of-flight	57.4	days
Maximum spacecraft acceleration	0.273	mm/s ²
Number of discretization nodes	200	NA

B. L2 NRHO to L1 Halo Transfer

Next, we demonstrate a transfer from an L2 Near Rectilinear Halo Orbit (NRHO) to an L1 Halo orbit. The initial conditions for the periodic orbits are in Table 6 and the problem parameters in Table 7. The NRHO is the 9:2 NRHO for the ongoing ARTEMIS program; the departure is from the apolune (southernmost point) of the NRHO, and the arrival is at one of the intersections between the L1 Halo and the xz -plane. The reference trajectory and control profile are shown in Fig. 5. The process of obtaining the reference trajectory is similar to the previous example; however, since this transfer features a close pass to the moon, the indirect method *regularizes* the equations of motion based on [41] to avoid the singularity in the inverse-square law. Furthermore, since the spacecraft's thrust capability is lower, we convert the minimum-energy trajectory to a fuel-optimal trajectory by setting a high-thrust magnitude and gradually lowering the magnitude, for each step solving the deterministic trajectory optimization problem with SCvx* using the previous solution as the initial guess.



(a) Trajectory xy and xz projection

First, we remark on some characteristics of the reference trajectory. The trajectory can be divided into three phases,

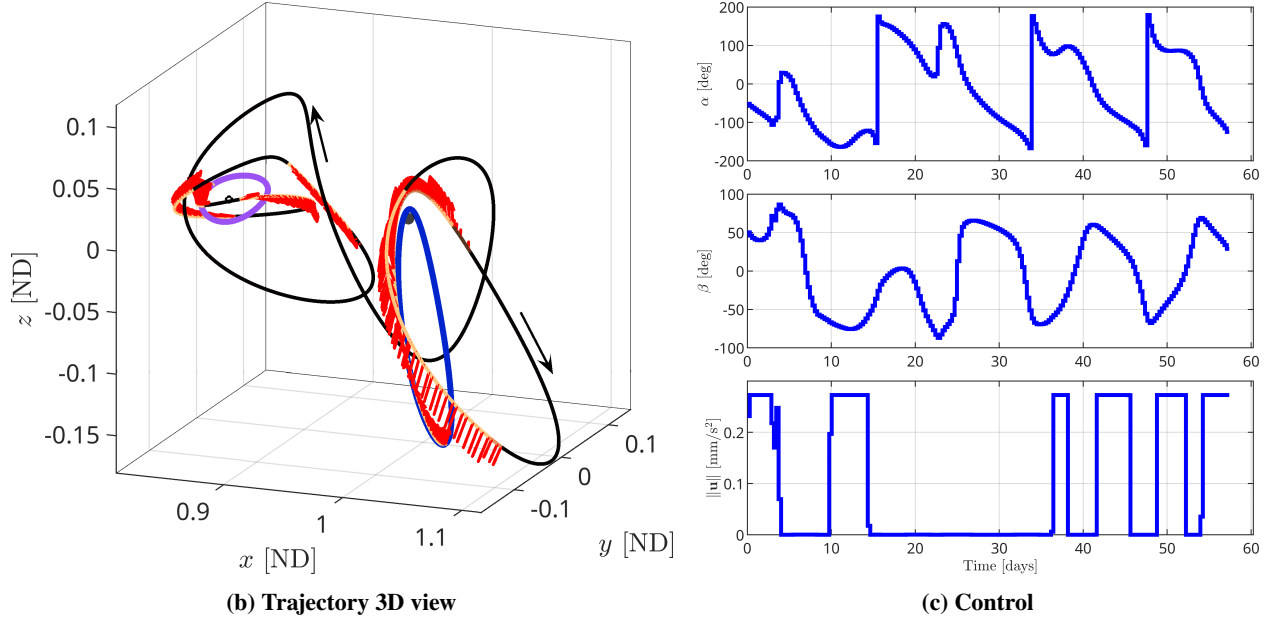
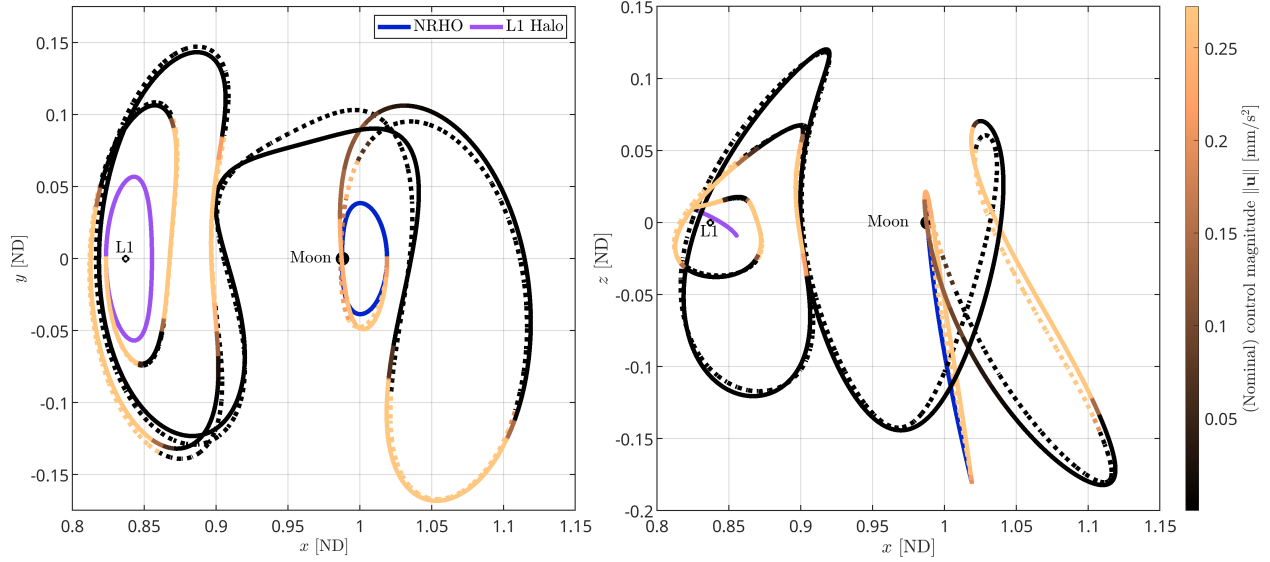


Fig. 5 Reference fuel-optimal L2 NRHO to L1 Halo transfer.

1. NRHO departure, 2. heteroclinic connection, and 3. Halo arrival. Visual inspection tells us that the first phase utilizes dynamical structures near the NRHO and resembles the P4HO2 family of periodic orbits [42, Fig. 9] that bifurcate from the NRHO. The second phase is a coasting phase, mirroring a heteroclinic connection. The final phase is the ‘spiral down’ towards the target Halo orbit. This phase seems to utilize the Lissajous orbit structures around the L1 point, and is similar to the one used in the ARTEMIS mission [43, Fig. 10], although the transfer here has larger inclination changes and features less revolutions. We remark that the trajectory optimization with SCP finds a trajectory that leverages the dynamical structures of the CR3BP without specific user inputs or dividing the transfer into multiple segments.

Next, we apply Algorithm 1 to the reference trajectory. In this scenario, we impose a maximum covariance constraint in order to maintain the validity of the linear covariance model. The algorithm converges in 60 iterations in 10 minutes. The larger number of iterations required compared to the previous example can be attributed to the higher nonlinearity in the lunar flyby phase and as a result, the noticeable change in the nominal solution from the initial reference; this transfer shows a larger discrepancy between the deterministic and robust trajectories compared to the DRO–DRO transfer. Figure 6 shows comparisons between the initial reference trajectory and the obtained nominal (mean) trajectory. We see notable differences between the two. As we see later, the robust trajectory devotes a significant amount of TC effort to shrink the state dispersion at the beginning of the transfer, especially since the lunar flyby phase is soon after the departure from the NRHO. Since the entire control term is bounded by the maximum control constraint, the nominal thrust magnitude is smaller than that of the deterministic trajectory. This is also reflected in the control profile in Fig. 9d. As a result, the robust trajectory especially has a larger movement in the y direction after the lunar flyby, and the heteroclinic connection uses a trajectory that is closer to the xz -plane. The difference in trajectories becomes smaller

as the spacecraft approaches the target Halo orbit.



(a) xy and xz projection. Broken lines show the trajectory from Fig. 5; solid lines show the robust trajectory.

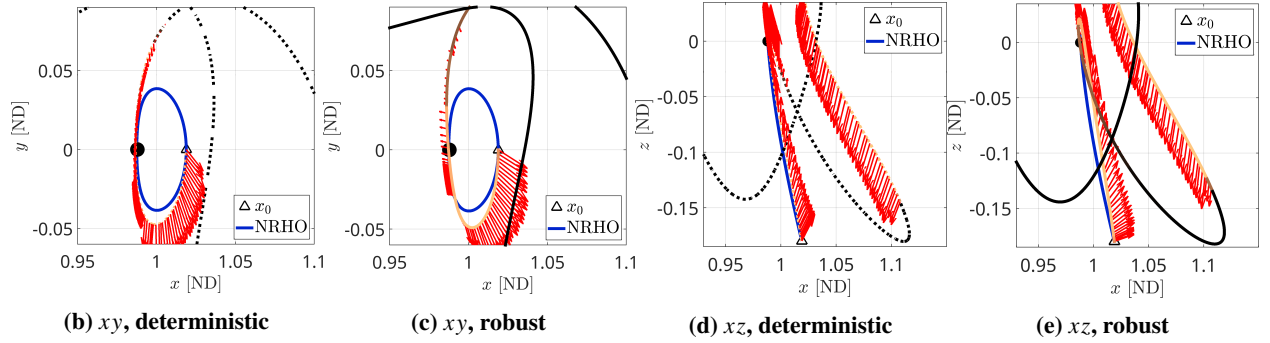


Fig. 6 Comparison of the deterministic vs robust trajectory. (a): Projections of both trajectories. (b)-(e): Zoomed in views of the trajectories and thrust vectors around the lunar flyby

Next, we observe the TC magnitudes along the trajectory. Figure 7 shows the TCM magnitudes (in log scale) along the trajectory ($\|K(\hat{x} - \bar{x})\|$). The largest TC magnitudes are, in order, the initial departure from the NRHO, the lunar flyby, and the final spiral down to the Halo orbit. To understand this, we observe the state standard deviations in Fig. 8. During the lunar flyby phase, the maximum covariance constraint is active in the velocity components, i.e. the diagonals of the covariance matrix that correspond to the velocity closely approach the corresponding indices of the maximum covariance matrix. As also verified in Section V.C, the trajectory passes through a highly error-sensitive region quickly after the lunar flyby, which explains the large TC magnitude leading up to this phase. The heteroclinic connection has small TC magnitudes as well as the nominal thrusting magnitude. Towards the end of the transfer, the TC magnitudes increase to satisfy the final covariance constraint.

Again, we perform Monte Carlo simulations with 200 samples. Figure 9 shows the results along with the derived

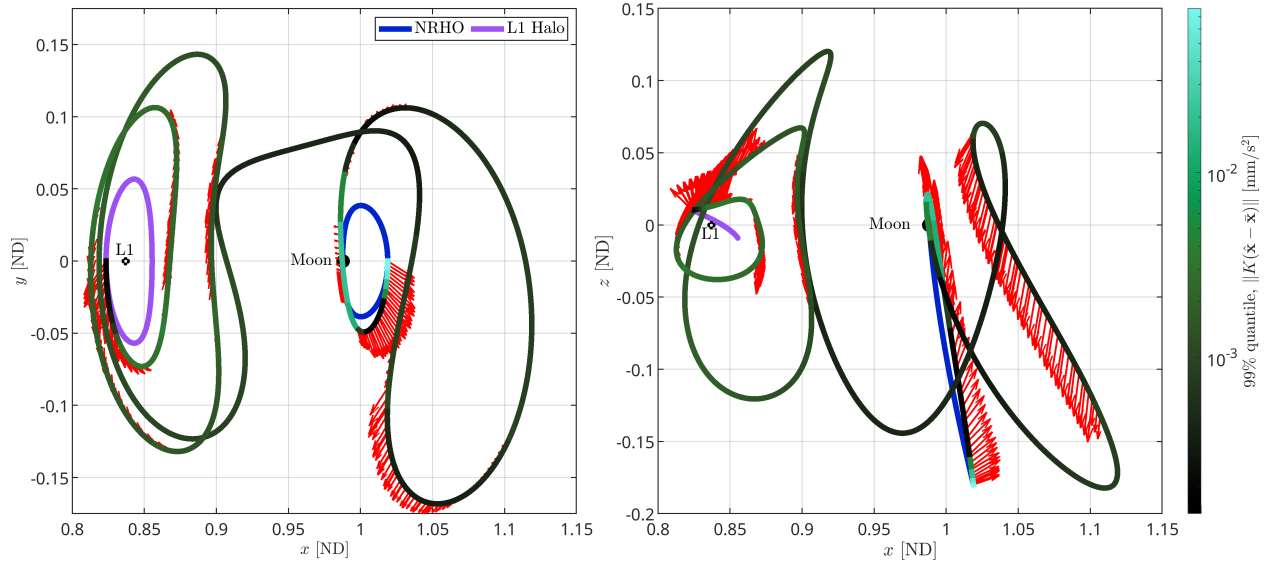


Fig. 7 Quantile trajectory correction magnitudes along the trajectory; red arrows show the magnitude of the nominal thrust acceleration

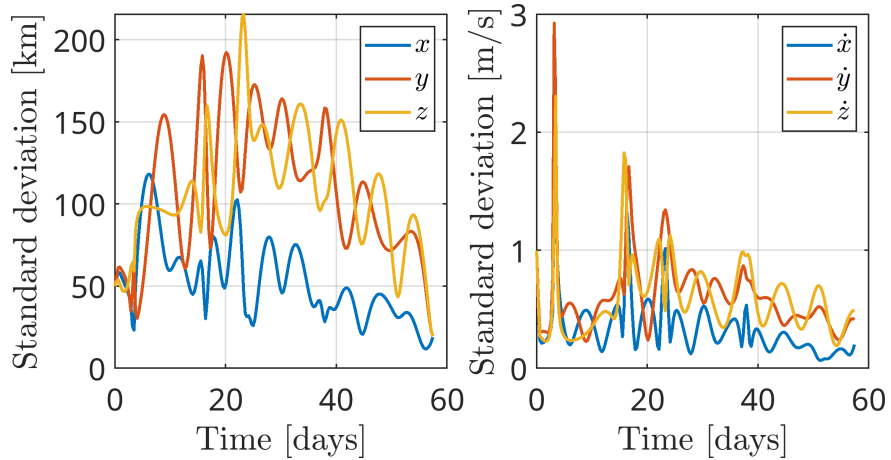
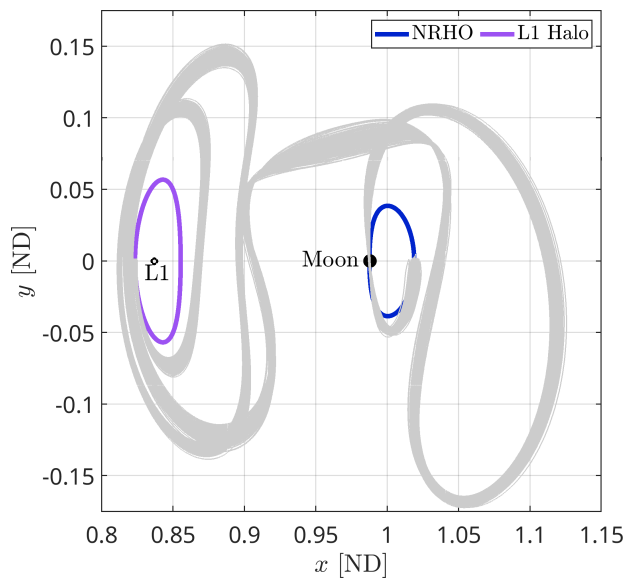
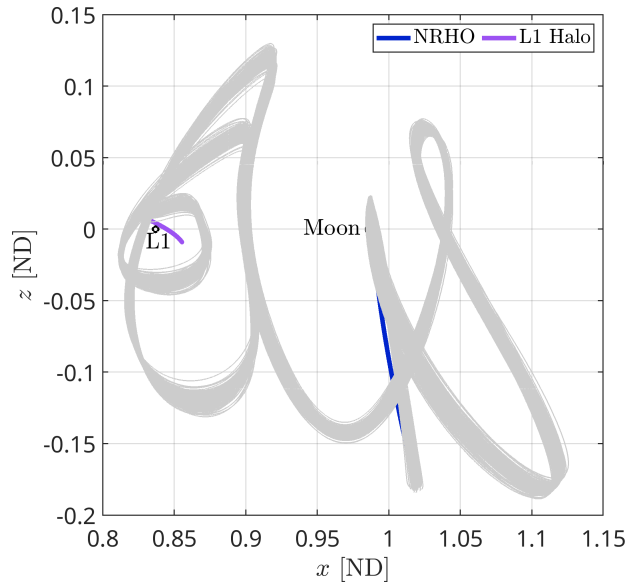


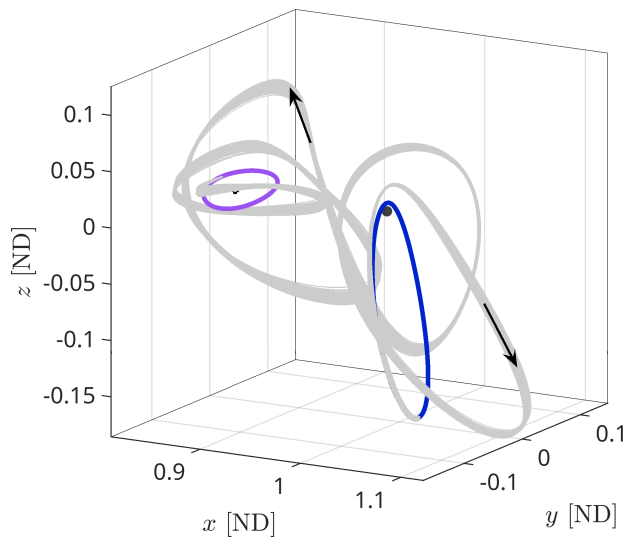
Fig. 8 State standard deviations (Square root of diagonals of P) for NRHO–Halo transfer



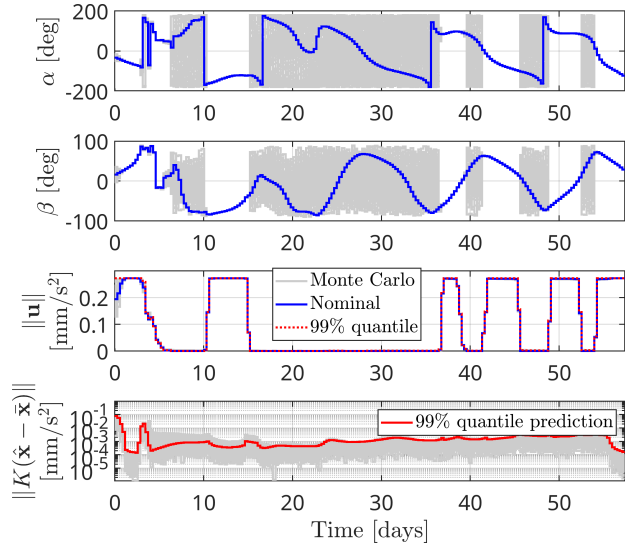
(a) Trajectories (xy projection, Deviations enlarged 10x)



(b) Trajectories (xz projection, Deviations enlarged 10x)



(c) Trajectories (xz projection, Deviations enlarged 5x)



(d) Control profile

Fig. 9 Monte Carlo simulation results for NRHO–Halo transfer.

control policy. Figures 9a,9b, and 9c show the trajectories of the Monte Carlo samples. Around the lunar flyby, the samples are tightly bound thanks to the TCs. Recall that the maximum covariance constraint is active during this period of the transfer. Note that in this problem setting, setting the largest covariance constraint is crucial for the success of the algorithm; without this constraint, the state dispersion can grow outside the region where linear covariance propagation is a valid approximation of the Fokker-Planck equation, resulting in the Monte Carlo samples escaping the cislunar region even if the SCP process converges. We also observe that the deviation expands near the heteroclinic connection, where the TC magnitude is minimal. This is an interesting phenomenon; it may be due to a dynamical structure, or it may simply be due to the heteroclinic connection being in the middle of the transfer, where efforts are not focused on satisfying the final covariance constraint. Observing the control profile in Fig. 9d, we see that, as observed in Fig. 7, the TC magnitude is largest at the beginning of the transfer. and around day 4, corresponding to the lunar flyby. Note that for a short duration around this time, the Monte Carlo samples violate the quantile prediction, i.e. the linear covariance model underestimates the control dispersion. This is likely due to the higher nonlinearity in the lunar flyby phase, which is not captured by the linear model. Nevertheless, the trajectory remains bounded, and the validity of the quantile prediction is restored after some time.

C. Analysis via Local Lyapunov Exponents

So far, we have observed that the CCDVO framework successfully provides optimized nominal (mean) trajectories as well as TCM policies. Our hypothesis is that the trajectories obtained with this framework are in general more robust regardless of the trajectory correction policy that is used. Here, we provide some analysis of the stability along the nominal trajectory computed from Algorithm 1 via the local Lyapunov exponent. The finite-time local Lyapunov exponent (LLE) is defined as [44]

$$\Lambda = \frac{1}{\Delta t} \ln \|\Phi(t + \Delta t, t_0)\|_2 = \frac{1}{\Delta t} \ln \sqrt{\lambda_{\max} \Phi(t + \Delta t, t_0) \Phi^T(t + \Delta t, t)} \quad (59)$$

with $\Phi(t + \Delta t, t)$ representing the state transition matrix from time t to $t + \Delta t$. While the horizon length Δt is a parameter which will effect the value of LLE, we have seen that the general trends in the LLE along the trajectory are fairly robust to the choice of Δt . For our analysis we choose Δt to be equal to the time step of the discretization.

Figure 10 shows the finite-time LLE plotted along the robust trajectory. Due to the large LLE value around the flyby, the trajectory is split into two parts for visualization. An immediate observation is the rise in LLE as the trajectory nears the xz -plane; when the spacecraft is closer to the moon, the gravitational influence of the moon is larger, leading to a higher LLE. Compare the plots with Fig. 7; the trends in Fig. 10a matches that of Fig. 7, with large TC efforts occurring around the flyby, and the sensitivity of this portion of the trajectory can be numerically verified through the LLE.

Finally, Fig. 11 shows the comparison of the LLE history between the deterministic and robust trajectories. We see

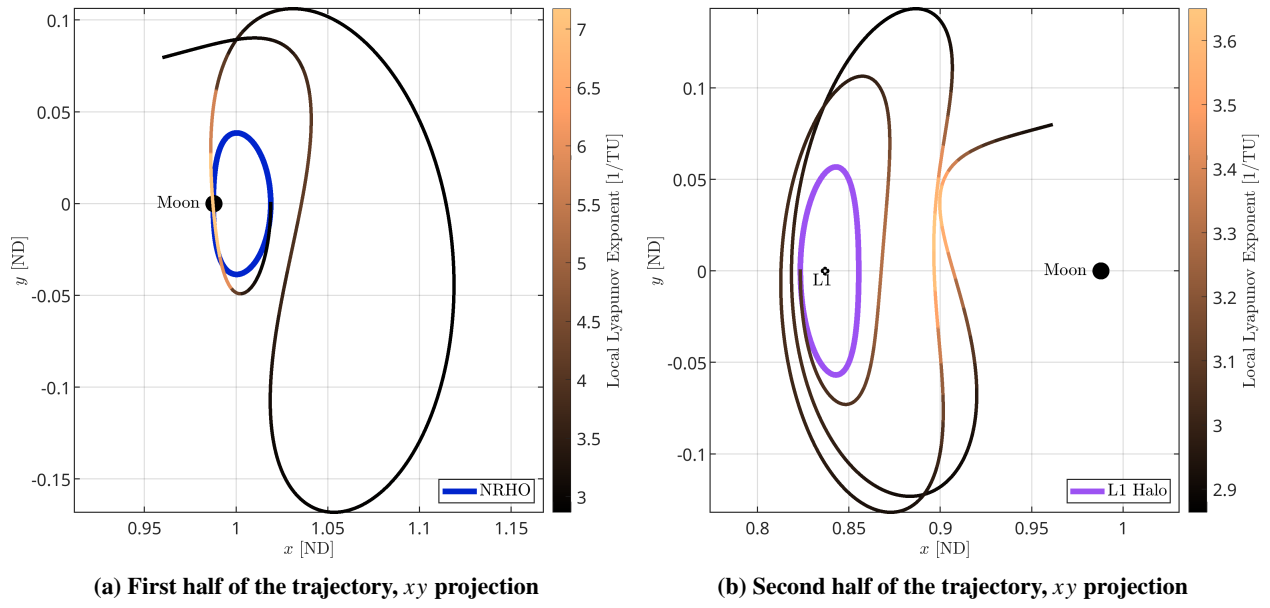


Fig. 10 Finite-time local Lyapunov exponent along the robust trajectory

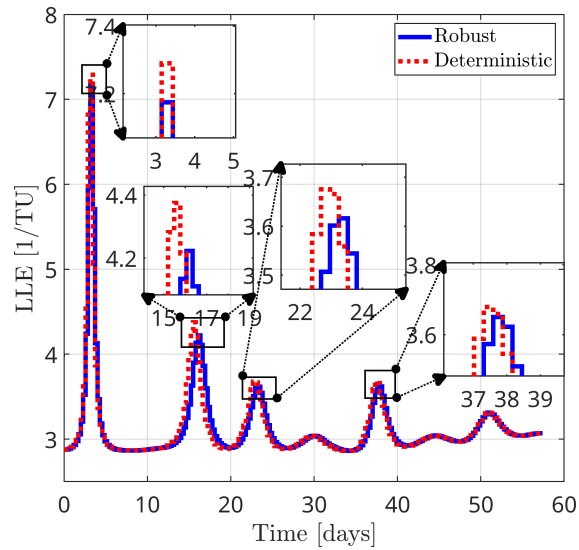


Fig. 11 Comparison of the local Lyapunov Exponent along the trajectory for the deterministic and robust trajectories

that the robust trajectory keeps the LLE peaks lower than the deterministic trajectory. This suggests that the nominal trajectory obtained from this framework is less sensitive to errors than the one obtained from the deterministic problem setting, *regardless of the trajectory correction policy used*; the LLE-based analysis is independent of the feedback gains, and the LLEs are computed based on the state transition matrix along the trajectory.

VI. Conclusions

This work presents sequential convex programming-based chance-constrained covariance steering for safe trajectory and controller design in cislunar space. First, we perform a thorough comparison of the recent advances in stochastic optimal control, highlighting each approach's unique capabilities. We show that various operational uncertainties and dynamics uncertainties can be incorporated into the optimization, which directly steers the underlying state distribution through computing optimal trajectory correction policies. Numerical examples of transfers between periodic orbits in the Earth-Moon Circular Restricted Problem demonstrate that this framework is applicable in the highly nonlinear cislunar region. Building on recent advances in the stochastic optimal control and robust space trajectory optimization literature, we formulate an algorithm that empirically achieves near-optimality for the nonlinear covariance steering problem, runs faster than previous methods by orders of magnitude, and can accommodate scaling issues unique to space trajectory optimization. Finally, local Lyapunov exponents are used to analyze the stability of the nominal trajectory, showing that the proposed method can provide a trajectory with better local stability properties than the deterministic counterpart.

VII. Acknowledgements

This material is based upon work supported by the Air Force Office of Scientific Research under award number FA9550-23-1-0512. N. Kumagai acknowledges support for his graduate studies from the Shigeta Education Fund. N. Kumagai thanks members of the Oguri Research Group for helpful discussions and Ethan Foss for pointing out the inverse-free discretization method.

References

- [1] Qi, D. C., and Oguri, K., "Analysis of Autonomous Orbit Determination in Various Near-Moon Periodic Orbits," *The Journal of the Astronautical Sciences*, Vol. 70, No. 6, 2023, p. 49. <https://doi.org/10.1007/s40295-023-00415-6>.
- [2] Sharan, S., Eapen, R., Singla, P., and Melton, R., "Accurate Uncertainty Characterization of Impulsive Thrust Maneuvers in the Restricted Three Body Problem," *The Journal of the Astronautical Sciences*, Vol. 70, No. 5, 2023, p. 35. <https://doi.org/10.1007/s40295-023-00394-8>.
- [3] Ozaki, N., Campagnola, S., Funase, R., and Yam, C. H., "Stochastic Differential Dynamic Programming with Unscented Transform for Low-Thrust Trajectory Design," *Journal of Guidance, Control, and Dynamics*, Vol. 41, No. 2, 2018, pp. 377–387. <https://doi.org/10.2514/1.G002367>.

- [4] Ozaki, N., Campagnola, S., and Funase, R., “Tube Stochastic Optimal Control for Nonlinear Constrained Trajectory Optimization Problems,” *Journal of Guidance, Control, and Dynamics*, Vol. 43, No. 4, 2020, pp. 645–655. <https://doi.org/10.2514/1.G004363>.
- [5] Yuan, H., Li, D., He, G., and Wang, J., “Uncertainty-resilient constrained rendezvous trajectory optimization via stochastic feedback control and unscented transformation,” *Acta Astronautica*, Vol. 219, 2024, pp. 264–277. <https://doi.org/10.1016/j.actaastro.2024.03.017>.
- [6] Greco, C., Campagnola, S., and Vasile, M., “Robust Space Trajectory Design Using Belief Optimal Control,” *Journal of Guidance, Control, and Dynamics*, Vol. 45, No. 6, 2022, pp. 1060–1077. <https://doi.org/10.2514/1.G005704>.
- [7] Jin, K., Geller, D. K., and Luo, J., “Robust Trajectory Design for Rendezvous and Proximity Operations with Uncertainties,” *Journal of Guidance, Control, and Dynamics*, Vol. 43, No. 4, 2020, pp. 741–753. <https://doi.org/10.2514/1.G004121>.
- [8] Cavesmith, T., Woffinden, D., and Collins, N., “Angles-Only Robust Trajectory Optimization for NRHO Rendezvous,” *46th Annual AAS Guidance, Navigation and Control (GN&C)*, Breckenridge, CO, 2024.
- [9] Margolis, B. W. L., and Woffinden, D., “Robust Trajectory Optimization Techniques Using a Sweeping Gradient Method and Linear Covariance Analysis,” *AAS/AIAA Astrodynamics Specialist Conference*, Broomfield, CO, USA, 2024.
- [10] Margolis, B. W. L., “A Sweeping Gradient Method for Ordinary Differential Equations with Events,” *Journal of Optimization Theory and Applications*, Vol. 199, No. 2, 2023, pp. 600–638. <https://doi.org/10.1007/s10957-023-02303-3>.
- [11] Oguri, K., and McMahon, J. W., “Stochastic Primer Vector for Robust Low-Thrust Trajectory Design Under Uncertainty,” *Journal of Guidance, Control, and Dynamics*, Vol. 45, No. 1, 2022, pp. 84–102. <https://doi.org/10.2514/1.G005970>.
- [12] Sidhoum, Y., and Oguri, K., “Robust Low-Thrust Trajectory Correction Planning Under Uncertainty: Primer Vector Theory Approach,” *AAS/AIAA Astrodynamics Specialist Conference*, Broomfield, CO, USA, 2024.
- [13] Ridderhof, J., Pilipovsky, J., and Tsiotras, P., “Chance-Constrained Covariance Control for Low-Thrust Minimum-Fuel Trajectory Optimization,” *AIAA/AAS Astrodynamics Specialists Conference*, South Lake Tahoe, CA, 2020.
- [14] Benedikter, B., Zavoli, A., Wang, Z., Pizzurro, S., and Cavallini, E., “Convex Approach to Covariance Control with Application to Stochastic Low-Thrust Trajectory Optimization,” *Journal of Guidance, Control, and Dynamics*, 2022, pp. 1–16. <https://doi.org/10.2514/1.G006806>.
- [15] Oguri, K., and Lantoine, G., “Stochastic Sequential Convex Programming for Robust Low-thrust Trajectory Design Under Uncertainty,” *AAS/AIAA Astrodynamics Specialist Conference*, AAS, Charlotte, NC, 2022.
- [16] Oguri, K., “Chance-Constrained Control for Safe Spacecraft Autonomy: Convex Programming Approach,” *2024 American Control Conference (ACC)*, Toronto, ON, Canada, 2024. <https://doi.org/10.23919/ACC60939.2024.10645008>.
- [17] Rapakoulias, G., and Tsiotras, P., “Comment on “Convex Approach to Covariance Control with Application to Stochastic Low-Thrust Trajectory Optimization”,” *Journal of Guidance, Control, and Dynamics*, Vol. 46, No. 5, 2023, pp. 1023–1024. <https://doi.org/10.2514/1.G007420>.

- [18] Liu, F., Rapakoulias, G., and Tsiotras, P., “Optimal Covariance Steering for Discrete-Time Linear Stochastic Systems,” , Jan. 2023. <https://doi.org/10.48550/arXiv.2211.00618>.
- [19] Pilipovsky, J., and Tsiotras, P., “Computationally Efficient Chance Constrained Covariance Control with Output Feedback,” , Oct. 2023. <https://doi.org/10.48550/arXiv.2310.02485>.
- [20] Zhang, Y., Cheng, M., Nan, B., and Li, S., “Stochastic Trajectory Optimization for 6-DOF Spacecraft Autonomous Rendezvous and Docking with Nonlinear Chance Constraints,” *Acta Astronautica*, Vol. 208, 2023, pp. 62–73. <https://doi.org/10.1016/j.actaastro.2023.04.004>.
- [21] Takubo, Y., and D’Amico, S., “Multiplicative Approach to Constrained Stochastic Attitude Control with Application to Rendezvous and Proximity Operations,” *AAS/AIAA Astrodynamics Specialist Conference*, Broomfield, CO, USA, 2024.
- [22] Ra, M. A. P., and Oguri, K., “Chance-Constrained Sensing-Optimal Path Planning for Safe Angles-Only Autonomous Navigation,” *AAS/AIAA Astrodynamics Specialist Conference*, Broomfield, CO, USA, 2024.
- [23] Balci, I. M., and Bakolas, E., “Density Steering of Gaussian Mixture Models for Discrete-Time Linear Systems,” *2024 American Control Conference (ACC)*, Toronto, ON, Canada, 2024, pp. 3935–3940. <https://doi.org/10.23919/ACC60939.2024.10644253>.
- [24] Kumagai, N., and Oguri, K., “Chance-Constrained Gaussian Mixture Steering to a Terminal Gaussian Distribution,” *2024 IEEE Conference on Decision and Control (CDC)*, Milan, Italy, 2024. <https://doi.org/10.48550/arXiv.2403.16302>.
- [25] Pavlak, T., “Trajectory Design and Orbit Maintenance Strategies in Multi-Body Dynamical Regimes,” Ph.D. thesis, Purdue University, 2013.
- [26] Gates, C. R., “A Simplified Model of Midcourse Maneuver Execution Errors,” Contractor Report JPL-TR-32-504, Jet Propulsion Lab, Pasadena, CA, 1963.
- [27] Kayama, Y., Howell, K. C., Bando, M., and Hokamoto, S., “Low-thrust trajectory design with successive convex optimization for libration point orbits,” *Journal of Guidance, Control, and Dynamics*, Vol. 45, No. 4, 2022, pp. 623–637. <https://doi.org/10.2514/1.G005916>.
- [28] Tapley, B. D., Schutz, B. E., and Born, G. H., *Statistical Orbit Determination*, Elsevier Academic Press, Amsterdam ; Boston, 2004. <https://doi.org/10.1016/B978-0-12-683630-1.X5019-X>.
- [29] Petersen, K. B., and Pedersen, M. S., “The Matrix Cookbook,” , Dec. 2012.
- [30] Boyd, S. P., and Vandenberghe, L., *Convex Optimization*, Cambridge University Press, Cambridge, UK ; New York, 2004. <https://doi.org/10.1017/CBO9780511804441>.
- [31] Rapakoulias, G., and Tsiotras, P., “Discrete-Time Optimal Covariance Steering via Semidefinite Programming,” *2023 62nd IEEE Conference on Decision and Control (CDC)*, 2023, pp. 1802–1807. <https://doi.org/10.1109/CDC49753.2023.10384118>.

- [32] MOSEK ApS, “The MOSEK optimization toolbox for MATLAB manual. Version 10.2.”, 2023. URL <https://docs.mosek.com/latest/toolbox/index.html>.
- [33] Lofberg, J., “YALMIP : a toolbox for modeling and optimization in MATLAB,” *2004 IEEE International Conference on Robotics and Automation*, 2004, pp. 284–289. <https://doi.org/10.1109/CACSD.2004.1393890>.
- [34] Oguri, K., “Successive Convexification with Feasibility Guarantee via Augmented Lagrangian for Non-Convex Optimal Control Problems,” *2023 62nd IEEE Conference on Decision and Control (CDC)*, IEEE, Singapore, Singapore, 2023, pp. 3296–3302. <https://doi.org/10.1109/CDC49753.2023.10383462>.
- [35] Oguri, K., and Lantoine, G., “Lossless Control-Convex Formulation for Solar-Sail Trajectory Optimization via Sequential Convex Programming,” *Journal of Guidance, Control, and Dynamics*, 2024. <https://doi.org/10.2514/1.G008361>, advance article.
- [36] Mao, Y., Szmuk, M., and Açıkmeşe, B., “Successive Convexification of Non-Convex Optimal Control Problems and Its Convergence Properties,” *2016 IEEE 55th Conference on Decision and Control (CDC)*, Las Vegas, NV, 2016, pp. 3636–3641. <https://doi.org/10.1109/CDC.2016.7798816>.
- [37] Lantoine, G., and Russell, R. P., “A Hybrid Differential Dynamic Programming Algorithm for Constrained Optimal Control Problems. Part 1: Theory,” *J Optim Theory Appl*, Vol. 154, No. 2, 2012, pp. 382–417. <https://doi.org/10.1007/s10957-012-0039-0>.
- [38] Kumagai, N., and Oguri, K., “Sequential Chance-Constrained Covariance Steering for Robust Cislunar Trajectory Design Under Uncertainties,” *AAS/AIAA Astrodynamics Specialist Conference*, Broomfield, CO, USA, 2024. <https://doi.org/10.2514/1.G008107>.
- [39] Okamoto, K., and Tsiotras, P., “Optimal Stochastic Vehicle Path Planning Using Covariance Steering,” *IEEE Robotics and Automation Letters*, Vol. 4, No. 3, 2019, pp. 2276–2281. <https://doi.org/10.1109/LRA.2019.2901546>.
- [40] Arya, V., Taheri, E., and Junkins, J., “Hyperbolic-Tangent-Based Smoothing with State Transition Matrix Implementation for Generating Fuel-Optimal Trajectories,” *AAS/AIAA Astrodynamics Specialist Conference*, AAS, Maui, HI, 2019.
- [41] Oguri, K., “Regularization of the Circular Restricted Three-Body Problem for Trajectory Optimization,” *AAS/AIAA Astrodynamics Specialist Conference*, Broomfield, CO, USA, 2024.
- [42] Zimovan-Spreen, E. M., Howell, K. C., and Davis, D. C., “Near Rectilinear Halo Orbits and Nearby Higher-Period Dynamical Structures: Orbital Stability and Resonance Properties,” *Celest Mech Dyn Astr*, Vol. 132, No. 5, 2020, p. 28. <https://doi.org/10.1007/s10569-020-09968-2>.
- [43] Sweetser, T. H., Broschart, S. B., Angelopoulos, V., Whiffen, G. J., Folta, D. C., Chung, M.-K., Hatch, S. J., and Woodard, M. A., “ARTEMIS Mission Design,” *The ARTEMIS Mission*, edited by C. Russell and V. Angelopoulos, Springer, New York, NY, 2014, pp. 61–91. https://doi.org/10.1007/978-1-4614-9554-3_4.

- [44] Anderson, R., Lo, M., and Born, G., "Application of Local Lyapunov Exponents to Maneuver Design and Navigation in the Three-Body Problem," *AAS/AIAA Astrodynamics Specialist Conference*, Big Sky, MT, 2003.